Materials Advances

ROYAL SOCIETY OF CHEMISTRY

PAPER

View Article Online
View Journal | View Issue

Cite this: *Mater. Adv.*, 2025, 6, 8034

Cationic iridium(III) complexes with a halogen-substituted pyridylbenzimidazole ancillary ligand for photodynamic therapy

Pierre-Henri Lanoë, *[a] Frédérique Loiseau,[a] Christian Philouze,[a] Camille Latouche, [bc] Laetitia Vanwonterghem,[d] Louis Biancon, [a] Ahmed S. Faihan, [a] Florian Molton,[a] Matéo Lavaud,[d] Anne-Laure Bulin,[d] Jean-Luc Coll, [d] Akos Banyasz [e] and Amandine Hurbin *[d]

Photodynamic therapy (PDT) is a powerful technique, as the oxidative stress generated by light irradiation induces cell death through apoptosis and necrosis. In type II PDT, iridium(III) complexes exhibiting high singlet oxygen quantum yields are potent photosensitizers (PS). Their emission properties under aerated conditions also make them valuable theranostic agents for imaging-guided PDT against cancer. We report a series of four cationic Ir(III) complexes featuring a 2-pyridylbenzimidazole ancillary ligand substituted at the 5′ position of the pyridinyl ring with a halogen atom (F, Cl, or Br), along with a halogen-free reference compound. The absorption and emission spectra are efficiently tuned by the electron-withdrawing ability of the halogen atoms, allowing the emission energy of one complex to reach the tissue transparency window. Two-photon absorption (TPA) spectra have been measured, and all complexes display a TPA maximum around 700 nm. All compounds efficiently generate both singlet oxygen ($^1O_2$) and superoxide anion ($O_2^{\bullet-}$). Cellular studies have shown that the complexes are rapidly internalized into mitochondria, produce reactive oxygen species ($^1O_2$ and $O_2^{\bullet-}$), and exhibit high phototoxicity, with IC_{50} values as low as 59.9 nM under low light fluence (1.2 J cm^{-2}). These results are supported by Time-Dependent Density Functional Theory (TD-DFT) simulations performed in both ground and excited states.

Received 27th August 2025,
Accepted 22nd September 2025

DOI: 10.1039/d5ma00964b

rsc.li/materials-advances

Introduction

Since the early 2000s, phosphorescent iridium(III) complexes have occupied a place of choice in modern photochemistry for a large number of applications, such as emissive materials in optoelectronics,[1–4] sensors, and luminescent biological probes for confocal microscopy.[5–8] Their high photoluminescence quantum efficiency, good electrochemical stability and reversibility, as well as synthesis by reliable and robust methods, have made these complexes accessible and effective. In addition, the tunability of the emission color, which spans from blue to near-infrared, is easily achieved by judicious modification of the ligands.[9–18] Finally, the triplet nature of their excited states has made them suitable and efficient photosensitizers (PS) for type I and type II photodynamic therapy (PDT), as well as for photocatalysis.[19,20] The majority of the cationic iridium(III) complexes reported to date derive from the archetypical complex: 2,2′-dipyridyl-bis[2′,4′-phenylpyridine]iridium(III) ($[(ppy)_2Irbpy]^+$, with ppy = 2′,4′-phenylpyridine and bpy = 2,2′-dipyridine, referred to as $[(ppy)_2Irbpy]$ hereafter).[21–23] The highest occupied molecular orbital (HOMO) for $[(ppy)_2Irbpy]$ typically receives contributions from both an Ir(III) d-orbital and from the π-system of the aryl rings of the cyclometallating ligands, while the lowest unoccupied molecular orbital (LUMO) has primarily π*-character localized on the ancillary ligand. The lowest-lying excited state of this family of complexes is usually described as a triplet metal-to-ligand charge transfer (^{3}MLCT*) admixed with ligand-to-ligand charge transfer (ancillary-based, ^{3}L′LCT*, L = bpy or ancillary ligands and L′ = cyclometallated ligand) excited state, resulting in a broad emission profile.[9,21,24,25]

The luminescence properties of Ir(III) complexes, combined with good-to-high singlet oxygen generation in type II PDT,

[a] Univ. Grenoble Alpes, CNRS, DCM, 38000 Grenoble, France. E-mail: pierre-henri.lanoe@univ-grenoble-alpes.fr
[b] Institut des Matériaux de Nantes Jean Rouxel, IMN, Nantes Université, CNRS, F-44000 Nantes, France
[c] Institut Universitaire de France (IUF), F-75005 Paris, France
[d] Institute for Advanced Biosciences, Univ. Grenoble Alpes, INSERM U1209, CNRS UMR5309, 38000 Grenoble, France. E-mail: amandine.hurbin@univ-grenoble-alpes.fr
[e] Laboratoire de Chimie École Normale Supérieure de Lyon, ENS, CNRS, UCBL UMR 5182, 46 Allée d'Italie, Lyon, 69364, France

have made these compounds potential candidates as theranostic agents for image-guided surgery and anti-cancer PDT.[26–29] Indeed, most of these complexes display phosphorescence quantum yields of around 2–10% in the presence of oxygen, which is intrinsically easy to distinguish from fluorescence due to their longer lifetimes (hundreds of ns *vs.* a few ns).[9] Using Ir(III) complexes as theranostic agents implies the ability to selectively target tumours. To achieve selectivity towards cancer cells, we aim to exploit their slightly more negative membrane potentials, which makes them more prone to accumulate lipophilic cations compared to healthy cells. This enhances the preferential uptake of cyclometallated Ir(III) complexes into cancer cells.[30] In addition, tumour cell targeting can also be achieved using nanoparticles obtained by self-assembly of Ir(III) complexes or by doping organic nanoparticles with an Ir(III) complex.[31–36] The main limitation of Ir(III) complexes in PDT lies in the wavelength required for their excitation, which generally falls outside the therapeutic window (600–1300 nm). Two-photon absorption (TPA) active molecules typically consist of a donor (D) and an acceptor (A) and are structured as dipolar or quadrupolar compounds, the latter being recognized as the most efficient.[37] Metal complexes exhibiting a charge-transfer (CT) transition from the metal to an electron-accepting ligand, such as cationic Ir(III), are suitable for TPA without requiring special molecular engineering.[20]

In the context of PDT, we designed a series of four cationic cyclometallated iridium(III) complexes, **Ir-X** with X = H, F, Cl, and Br, featuring a 2-pyridylbenzimidazole ancillary ligand bearing the halogen atom at the 5′ position of the pyridyl ring, in order to tune the photophysical properties, the LUMO of these complexes being mainly localized on the diimine ligand.[21] These complexes were fully characterized using nuclear magnetic resonance (NMR) spectroscopy, high-resolution mass spectrometry, luminescence spectroscopy, two-photon absorption, and studied by density functional theory (DFT) computations. Their cellular uptake and localization, as well as their ability to generate cellular reactive oxygen species (ROS) and act as photosensitizers (PS) for PDT, were then evaluated.

Results and discussion

Synthesis

The synthesis of the 2-(5′-halogenatedpyridinyl)benzimidazole ligands followed our previously reported two-step synthesis procedure on 2-phenylbenzimidazole (Fig. 1).[38,39] First, a nucleophilic aromatic substitution took place between 4-fluoro-3-nitrotoluene and *n*-butylamine in DMSO at 60 °C. After extraction, the desired product **1** was obtained in high yield (97%) without further purification. Ligands **2a–d** were obtained by a condensation reaction between compound **1** and the appropriate formylpyridine in a methoxyethanol/water mixture, with an excess of the reductant sodium metabisulfite, and the mixture was refluxed overnight. The reaction was quenched by addition of water, followed by extraction, and the pure compounds **2a–d** were obtained after flash chromatography on silica gel, except for **2a**, which was obtained pure after extraction and solvent evaporation. The complexes were synthesized by reacting the desired ligand with di-μ-chloridotetrakis[2-pyridinylphenyl]-diiridium(III) in a MeOH/CH_2Cl_2 mixture heated under reflux

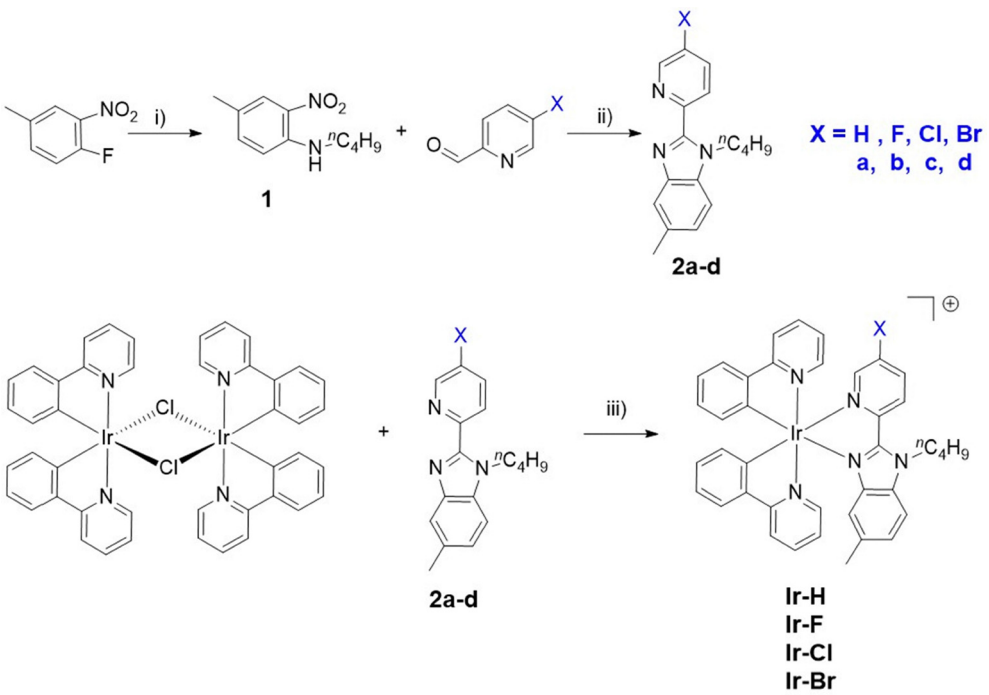

Fig. 1 Synthesis of ligand **2a–d** and complexes **Ir-H**, **F**, **Cl**, **Br**. (i) DMSO, 60 °C overnight; (ii) $Na_2S_2O_5$, H_2O/MeOEtOH reflux overnight; (iii) CH_2Cl_2/MeOH reflux overnight then KPF_6(sat).

overnight. At room temperature (r.t.), the reaction mixture was concentrated, and a solution of KPF_6 was added, leading to precipitation of the complexes. The crude complexes were recovered by filtration and purified by simple recrystallization, preceded by filtration over Celite®. Complexes and ligands were fully characterized by high-resolution mass spectrometry and ^1H, ^{13}C, and ^{19}F NMR when appropriate. The spectra are displayed in the SI (Fig. S1–S13).

Structural characterizations

X-ray diffraction quality crystals were obtained by slow vapor diffusion of diisopropyl ether into a concentrated solution of a complex (**Ir-H** or **Ir-Cl**) in acetonitrile. The X-ray crystal structures are presented in Fig. 2, and the crystal data and structure refinement are given in Table S1. Both **Ir-H** and **Ir-Cl** crystallized in a monoclinic Bravais lattice with space group $P2_1/c$, and the asymmetric units display a single complex with the counterion and a molecule of acetonitrile. In addition, both Δ and Λ isomers are present in the lattice, as they are formed in a 1 : 1 ratio during the cyclometallation step.[40,41] Both complexes exhibit an octahedral geometry around the metal center, with slight distortion, as illustrated by the N1–Ir–N2 angle of approximately 172° (Table 1). The bond lengths observed in the two complexes around the metal core are similar, along with the corresponding angles: Ir–N1/2 ∼2.045 Å, Ir–C1/2 ∼2.012 Å, and Ir–N3/4 ∼2.151 Å. It is worth noting that the latter bond lengths are longer than Ir–N1/2 due to the *trans* effect, which results from the strong σ-donating ability of the cyclometallating carbon atoms.[24] Additionally, both **Ir-H** and **Ir-Cl** exhibit a weak distortion angle between the pyridyl and benzimidazole mean planes, measured at 3.38° and 2.85°, respectively.

Absorption and emission spectroscopy

The absorption properties of the four complexes were investigated in a dilute solution of CH_2Cl_2 under air at 298 K. The data are gathered in Table 2, the spectra in Fig. 3, and individual absorption and emission spectra are displayed in Fig. S14. Compared with similar complexes already reported,[22,42–44] the absorption spectra of the compounds can be divided into three main spectral regions. In the UV region (250–340 nm), intense absorption bands are observed, corresponding to spin-allowed π–π* ligand-centered transitions (^{1}LC), which can be attributed to both the cyclometallating and the chelating ligands. In the second region, ranging from 320 to 480 nm, moderate to low absorption bands are assigned to spin-allowed metal-to-ligand charge transfer (^{1}MLCT) transitions (L = ancillary ligand), admixed with ligand-to-ligand charge transfer (^{1}L′LCT, with L′ = cyclometallated ligand) transitions from the cyclometallating ligand to the π* orbital of the ancillary ligand. The third region, above 490 nm, shows a very weak absorption tail, which can be attributed to direct absorption from the ground state to the ^{3}MLCT/^{3}L′LCT excited states. This transition is partially allowed due to the high spin–orbit coupling constant of the iridium core (ζ = 3909 cm^{-1}).[9] The absorption spectra of the four complexes are similar and only slightly influenced by the nature of the substituent at the 5′ position of the pyridine ring. For example, the absorption band around 345 nm, corresponding to MLCT or L′LCT transitions, is gradually red-shifted (bathochromic shift) from 340 nm for **Ir-H** to 355 nm for **Ir-Br**, following the electron-withdrawing effect of the halogen atom. It is possible to correlate the absorption and/or emission energy (see below) with the Hammett parameter,[38,45,46] although it has more commonly been applied to oxidation potentials.[42,47,48] Assuming that the substituent mainly affects the LUMO localized on the pyridylbenzimidazole ligand, the absorption energy shows a linear correlation with the Hammett parameter σ_{para} (Fig. S15).

The emission properties of the complexes were investigated in dilute CH_2Cl_2 solutions under air-equilibrated and deaerated conditions at 298 K, as well as in a rigid butyronitrile matrix at 77 K (Fig. 3A and Fig. S14, S16). All the complexes displayed broad emission in the orange-red region of the spectrum, with good to high quantum yields ranging from 0.23 to 0.87. The emission is highly sensitive to oxygen ($k[O_2]$ = 0.9–3.4 × 10^9 L mol^{-1} s^{-1}), with long emission lifetimes (τ = 623–1320 ns in deaerated solutions), confirming that the complexes are phosphorescent, as expected. The emission energies of the series show a linear dependence on the Hammett parameter

Table 1 Selected experimental and simulated (between square brackets) bond lengths and angles at the ground state of **Ir-H** and **Ir-Cl**

Parameter	Ir-H	Ir-Cl
Ir–N1 (Å)	2.044(3) [2.062]	2.051(4) [2.064]
Ir–N2 (Å)	2.045(3) [2.062]	2.040(4) [2.058]
Ir–N3 (Å)	2.170(3) [2.208]	2.164(4) [2.219]
Ir–N4 (Å)	2.130(3) [2.184]	2.142(3) [2.186]
Ir–C1 (Å)	2.011(4) [2.011]	2.007(4) [2.009]
Ir–C2 (Å)	2.014(4) [2.011]	2.017(4) [2.011]
N1^Ir^N2 (°)	171.6(1) [173.9]	172.0(2) [173.6]
C1^Ir^N1(°)	80.8(1) [80.1]	80.4(2) [80.1]
C2^Ir^N2 (°)	80.5(1) [80.1]	80.7(2) [80.2]
N3^Ir^N4 (°)	75.2(1) [75.2]	75.4(1) [75.0]
Ancillary ligand distortion[a] (°)	3.38 [3.41]	2.85 [2.25]

[a] The distortion is measured between the mean plan of the two heterocycles pyridyl and benzimidazole.

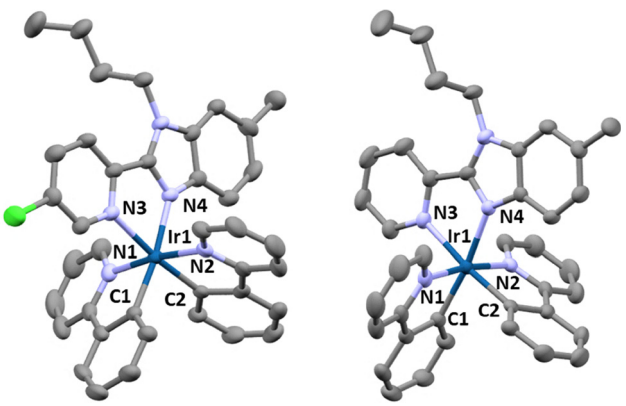

Fig. 2 X-ray crystalline structures of the complexes **Ir-Cl** (left) and **Ir-H** (right). Hydrogen atoms have been omitted for clarity.

Table 2 Spectroscopic data in CH_2Cl_2 at 298 K

Complex	Absorption ($\times 10^4$ L mol^{-1} cm^{-1})	λ_{em}/nm	Φ^{ab} [air]	τ^b/ns [air]	k_r 10^5 s^{-1}	Σk_{nr} 10^5 s^{-1}	$k[O_2]$ 10^9/L mol^{-1} s^{-1} ^{c}	Φ_Δ ^{d}
Ir-H	254 (4.5), 290 (2.8), 315 (2.5), 244 (2.8), 340 (2.8), 390 (0.9), 427 (0.3), 475 (0.1)	586	0.76 [0.08]	1260 [262]	6.0	1.9	1.4	0.78
Ir-F	254 (4.6), 300 (2.9), 341 (2.7), 346 (2.7), 368 (1.3), 378 (1.1), 467 (0.1)	589	0.87 [0.08]	1320 [213]	6.6	1.0	1.8	0.87
Ir-Cl	256 (5.3), 284 (2.7), 301 (2.3), 324 (2.4), 350 (2.9), 384 (1.4), 472 (0.1)	607	0.56 [0.09]	623 [290]	9.0	7.1	0.8	0.57
Ir-Br	257 (4.7), 302 (2.6), 340 (2.6), 355 (2.7), 388 (1.1), 416 (0.5), 470 (0.1),	610	0.23 [0.08]	918 [228]	2.5	8.4	1.5	0.66

^{a} $Ru[bpy]_3(PF_6)_2$ in CH_3CN was used as reference. ^{b} Deaerated. ^{c} Estimated from $\frac{\tau_0}{\tau} = 1 + k_q\tau[Q]$ with Q = $[O_2]$ = 2.2 mmol L^{-1} in CH_2Cl_2. ^{d} Singlet oxygen generation quantum yield obtained in $CHCl_3$ from Stern–Volmer plot using phenalenone as standard with Φ_Δ = 0.98 in $CHCl_3$.

σ_{para} of the halogen atom at the 5′ position of the ancillary ligand, indicating that the substituent influences the energy of the lowest unoccupied molecular orbitals (*i.e.*, the LUMO). All four complexes exhibit strong rigidochromism at 77 K (Fig. S16), indicating that the emission arises from the radiative deactivation of a MLCT/L′LCT triplet excited state to the singlet ground state. This behaviour is typical of this family of cationic Ir(III) complexes, where the frontier orbitals are generally localized on the metal and the cyclometallating ring for the HOMO, and on the neutral ancillary ligand for the LUMO,[9,21] as confirmed by theoretical investigations (see below). The ability of the four complexes to generate singlet oxygen *via* energy transfer was investigated by direct observation of $^1O_2$ phosphorescence at 1275 nm in chloroform solution, using phenalenone as a standard. The complexes exhibit good to high quantum yields of singlet oxygen generation, ranging from 57% to 87%. Interestingly, the complexes, with the exception of **Ir-Br**, display Φ_Δ that match their phosphorescence quantum yield in deaerated solutions, indicating highly efficient energy transfer between the complexes and $^3O_2$. Φ_Δ is correlated with the efficiency of intersystem crossing (ISC), which is considered to be unity in Ir(III) complexes. **Ir-Br** appears to behave differently, as its Φ_Δ (66%) is higher than its phosphorescence quantum yield (23%). This can be rationalized by its particular sensitivity to O_2, since its $k[O_2]$ is of the same order of magnitude as that of **Ir-H** and **Ir-F**, which display the highest Φ_Δ values. Furthermore, it is known that polar solvents can enhance singlet electron transfer to $^3O_2$, leading to the formation of superoxide radical anion $O_2^{\bullet-}$.[49] To investigate this, the complexes were dissolved in methanol with 5,5-dimethyl-1-pyrroline N-oxide (DMPO), a spin trap known to form an adduct with $O_2^{\bullet-}$. Electron paramagnetic resonance (EPR) signals were recorded before and after illumination at 420 nm (Fig. 3B). All **Ir-X** complexes clearly generate $O_2^{\bullet-}$ in polar media, as evidenced by the characteristic DMPO–$O_2^{\bullet-}$ adduct signal (Fig. S17).

Theoretical investigation

As presented in Table 1, the calculated bond lengths and angles for **Ir-H** and **Ir-Cl** complexes are in excellent agreement with the experimental data. Notably, the simulations accurately capture the shortening of Ir–N2 and the lengthening of Ir–N1 as one transition from **Ir-H** to **Ir-Cl**. These findings on ground-state structures give confidence in the assessment of the electronic structure of the complexes. Given the similarity of electronic structures across all complexes, this part will focus on the specific characteristics of **Ir-H** (see Fig. S18). The Highest Occupied Molecular Orbitals (HOMOs) are predominantly localized on the metallic center, with a noteworthy contribution from the phenylpyridine moieties. The lowest unoccupied molecular orbital (LUMO) is strictly localized on the ancillary ligand, while LUMO+1 and LUMO+2 primarily reside on the phenylpyridine moiety. It is worth noting that for **Ir-X** (X = halogens), LUMO+2 includes a non-negligible ancillary contribution. Fig. 3C and D explicitly illustrates that as one progresses from **Ir-H** and **Ir-F** to larger terminal halides (X = Cl, Br, and hypothetical I), the bandgap diminishes the LUMO stabilization.

To attribute absorption bands with wavelengths exceeding 400 nm, time-dependent density functional theory (TD-DFT) computations were performed, and bands assignment and oscillator strength is displayed in Table S2. The simulated spectra align well with experimental results, showcasing numerous transitions in the 250–420 nm range. In all instances, the highest transition, occurring around 480–500 nm depending on the complex, features a very small oscillator strength ($f \approx 0.0005$) and corresponds to a charge transfer from the metal and phenylpyridine moieties to the ancillary ligand. Subsequently, a combination of two transitions is consistently computed with a larger oscillator strength (ranging from 0.04 to 0.10). These transitions involve shifts from HOMO, HOMO−1, and HOMO−2 to LUMO, LUMO+1, and LUMO+2, representing a mixture of ML′CT, LL′CT, and LLCT.

We now focus the discussion on the first triplet excited states (T_0) using the classical ΔSCF procedure (unrestricted), since it has been proven to be an accurate and efficient method for such transition metal complexes.[38,50,51] First, the simulation successfully reproduces the trend in the spectra between **Ir-H** and **Ir-F** *versus* **Ir-Cl** and **Ir-Br** (Fig. 3C). Moreover, the overall shape of the simulated spectra closely aligns with the experimental results. However, surprisingly, a systematic ∼0.20 eV electronic error exists between the theoretical and experimental maxima, as illustrated in Fig. 3E.

Given the correct overall trend, the consistent electronic error, and the overall well-simulated global band shape, our

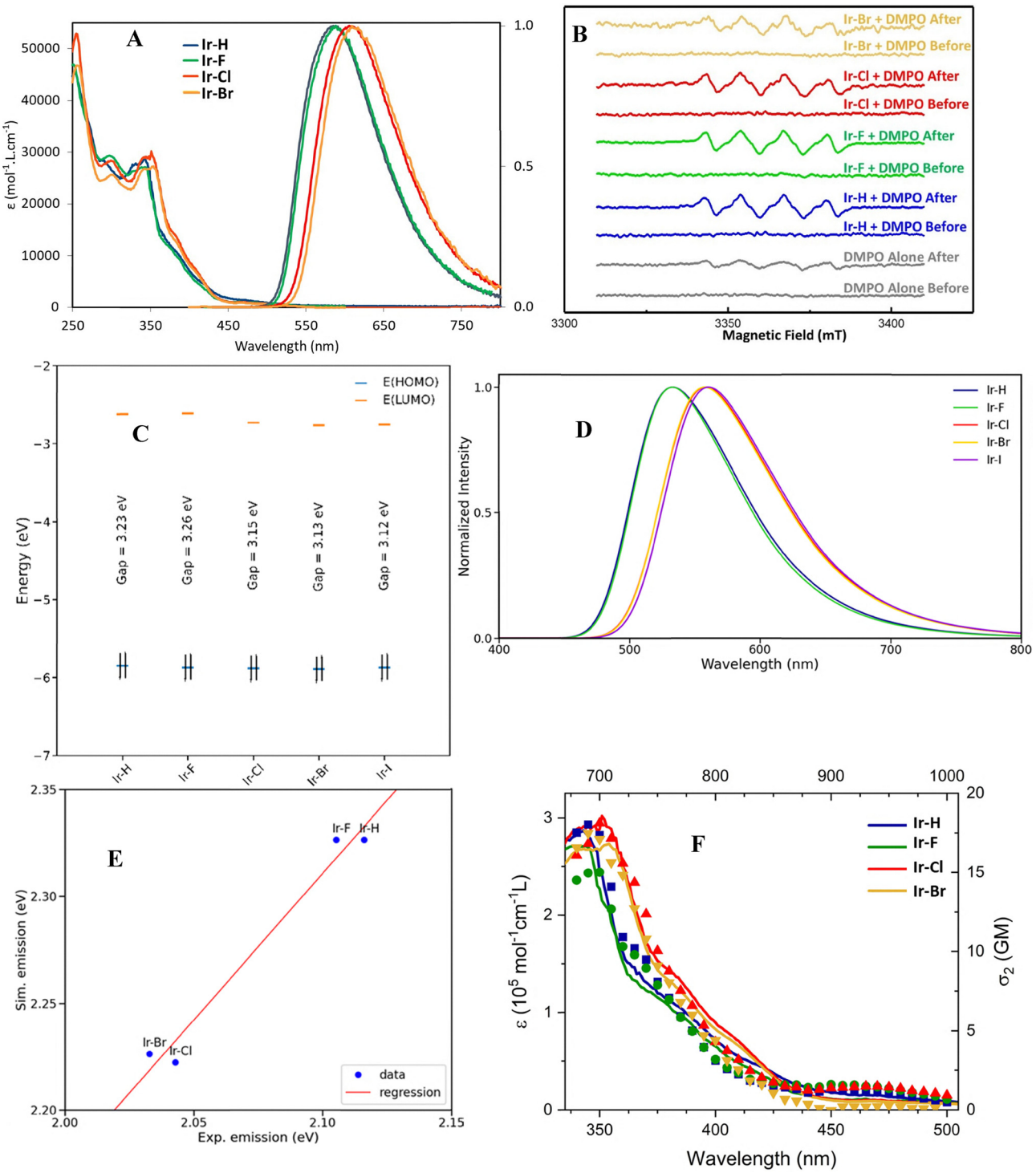

Fig. 3 (A) Absorption and normalized emission spectra in CH_2Cl_2 at r.t. (B) EPR spectra of **Ir-X** (0.1 mM) in presence of DMPO (60 mM) in MeOH before illumination and after 5 min blue light illumination (420 nm). (C) HOMO, LUMO and bandgap energies of the simulated complexes in the ground state. (D) Simulated spectra of **Ir-H**, **Ir-F**, **Ir-Cl**, **Ir-Br** and hypothetical **Ir-I**. (E) Correlation between experimental and theoretical maxima. (F) Two-photon absorption cross-section spectra of the **Ir-X** complexes measured in aerated dichloromethane solutions at room temperature.

confidence in the reliability of our simulations remains unchanged. We can now examine the localization of the electronic density in the excited state (see Fig. S19). As observed, the spin densities for all complexes are similar, with a concentrated density in the metal, the ancillary ligand, and the phenyl portion of the phenylpyridine moieties. This suggests the population of the LUMO, with a significant density transfer from the metal and phenylpyridine to the ancillary ligand.

Two-photon absorption

The two-photon absorption spectra and absolute two-photon absorption coefficients of the halogenated **Ir-X** compounds were measured by the two-photon excited fluorescence (TPEF) technique as described earlier.[52–54]

The two-photon absorption spectra of the **Ir-X** complexes along with their linear absorption spectra are shown in Fig. 3F and individual two-photon absorption spectra are displayed in Fig. S20. As can be seen, the two-photon absorption spectra show good overall overlap with their one-photon counterparts, the maxima of the two-photon absorption spectra peaking around 690 nm for all the four compounds with cross section value of about 17 GM for **Ir-H**, **Ir-Cl** and **Ir-Br**. The maximum two-photon absorption cross section is slightly lower for **Ir-F** (15 GM), but this difference is at the limit of the experimental accuracy of the TPEF method, which also depends on concentration accuracy and fluorescence quantum yield values. It is interesting to note that the ^{3}MLCT/^{3}L′LCT transition gives a very small, but significant contribution above 900 nm. This low energy absorption band is also observed in one-photon absorption (Fig. 3F).

Cellular uptake

We evaluated the four cationic cyclometallated Ir(III) complexes *in vitro*. Cellular uptake of the complexes was first assessed in two different human cancer cell lines and showed that all complexes were rapidly internalized into the cytoplasm of A549 and HeLa cells (Fig. 4A and Fig. S21). These results were confirmed by flow cytometry analyses: the peaks and mean fluorescence intensities were similar for all four complexes after 4 h, whereas they were strongly inhibited when incubated at 4 °C (Fig. 4B), suggesting that the complexes entered the cells *via* active internalization processes. **Ir-F** and **Ir-H** showed a slightly higher uptake than **Ir-Cl** and **Ir-Br**. Colocalization experiments with organelle-specific fluorescent dyes showed that the red fluorescent signal of all four complexes strongly overlapped with the mitochondria markers (Fig. 5 and Fig. S22), as previously observed with most Ir(III) complexes.[55] Mean Pearson's correlation coefficients were calculated to assess mitochondrial and lysosomal localization. For mitochondrial localization, values ranged from 0.607 to 0.728 in A549 cells and from 0.680 to 0.712 in HeLa cells (Fig. 5C). In contrast, lysosomal localization showed lower

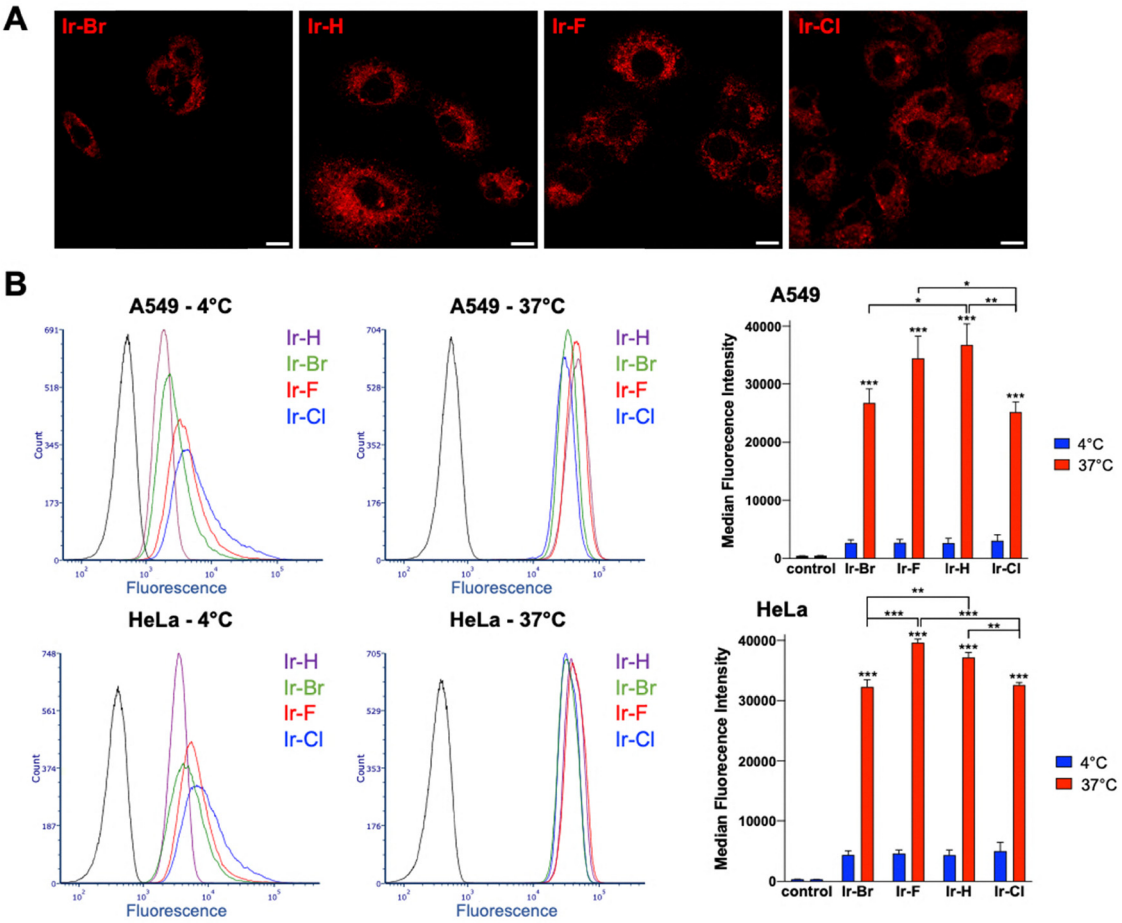

Fig. 4 Ir(III) complexes are efficiently internalized in human cancer cells. Cells were incubated with 1 μmol L^{-1} **Ir-Br**, **Ir-F**, **Ir-H**, and **Ir-Cl**. (A) Representatives confocal microscopy images of A549 cells after 4 h incubation. The compounds fluorescence is observed in red. Scale bars = 10 μm. (B) Flow cytometry analysis and corresponding quantitative results of the cellular uptake of compounds after 4 h at 4 °C or 37 °C. Data are expressed as mean ± SEM (n = 3). *, $p < 0.05$; **, $p < 0.01$; ***, $p < 0.001$; Two-way ANOVA with Tukey's multiple comparisons test.

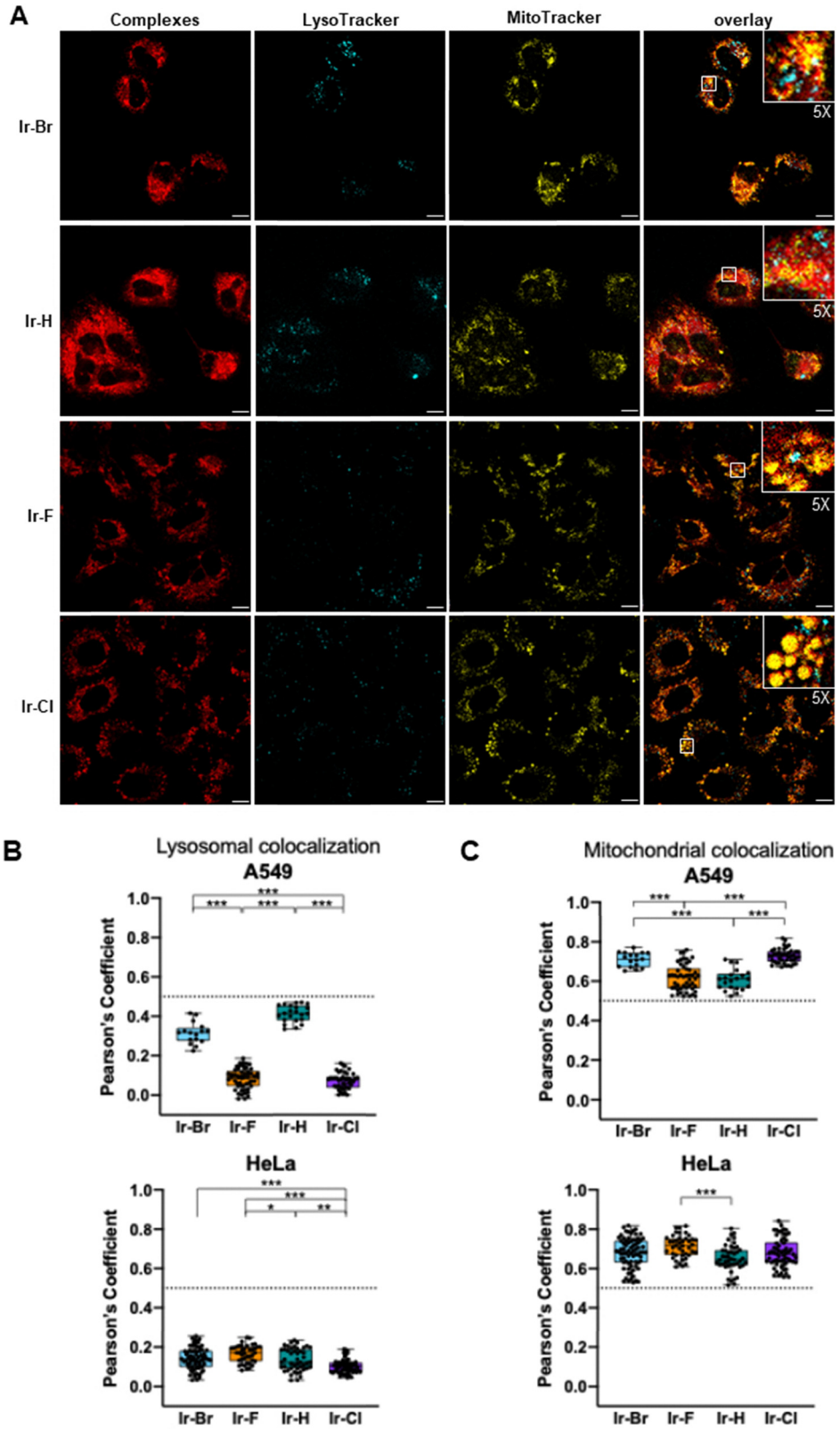

Fig. 5 Ir(III) complexes accumulate in mitochondria. (A) Confocal images showing the colocalization between the Ir complexes **Ir-Br**, **Ir-F**, **Ir-H**, or **Ir-Cl** incubated at 1 μmol L^{-1}, and organelle-specific probes (LysoTracker and MitoTracker) in A549 cells. Compounds fluorescence (red), MitoTracker orange (yellow), LysoTracker blue (cyan). Scale bars = 10 μm. (B) Pearson's correlation coefficients calculated from compounds and lysoTracker signal in A549 and HeLa cells. (C) Pearson's correlation coefficients calculated from compounds and mitoTracker signal. Data were obtained from individual cell quantification, with 16 to 74 cells analyzed per condition. *, $p < 0.05$; **, $p < 0.01$; ***, $p < 0.001$; Kruskal–Wallis test with Dunn's multiple comparison test.

Table 3 Sensitivity of cancer cells to Ir(III) complexes

		IC_{50} (nmol L^{-1})			
Cell lines	Light	**Ir-Br**	**Ir-H**	**Ir-F**	**Ir-Cl**
A549	Dark	104.3 ± 6.8	158.0 ± 10.2	126.5 ± 9.1	167.8 ± 12.4
	1.2 J cm^{-2}	70.5 ± 5.5	62.7 ± 3.8	59.9 ± 5.0	88.7 ± 6.2
	10 J cm^{-2}	17.2 ± 0.9	12.2 ± 0.7	12.0 ± 0.8	16.9 ± 1.3
HeLa	Dark	156.3 ± 8.6	230.1 ± 12.6	178.6 ± 12.1	163.3 ± 10.3
	1.2 J cm^{-2}	75.9 ± 2.2	72.5 ± 1.7	65.1 ± 2.1	74.7 ± 4.2
	10 J cm^{-2}	9.2 ± 0.4	8.4 ± 0.3	5.5 ± 0.2	11.1 ± 0.3

correlations, with values of r = 0.084–0.413 in A549 cells and r = 0.104–0.166 in HeLa cells (Fig. 5B). Finally, **Ir-Br** and **Ir-Cl** showed a slightly higher mitochondrial localization than **Ir-H** and **Ir-F** in A549 cells.

Phototoxicity

We investigated the phototoxicity of Ir(III) complexes in cells. We have previously shown that illumination at 420 nm, in the absence of the compounds, induced only a moderate level of

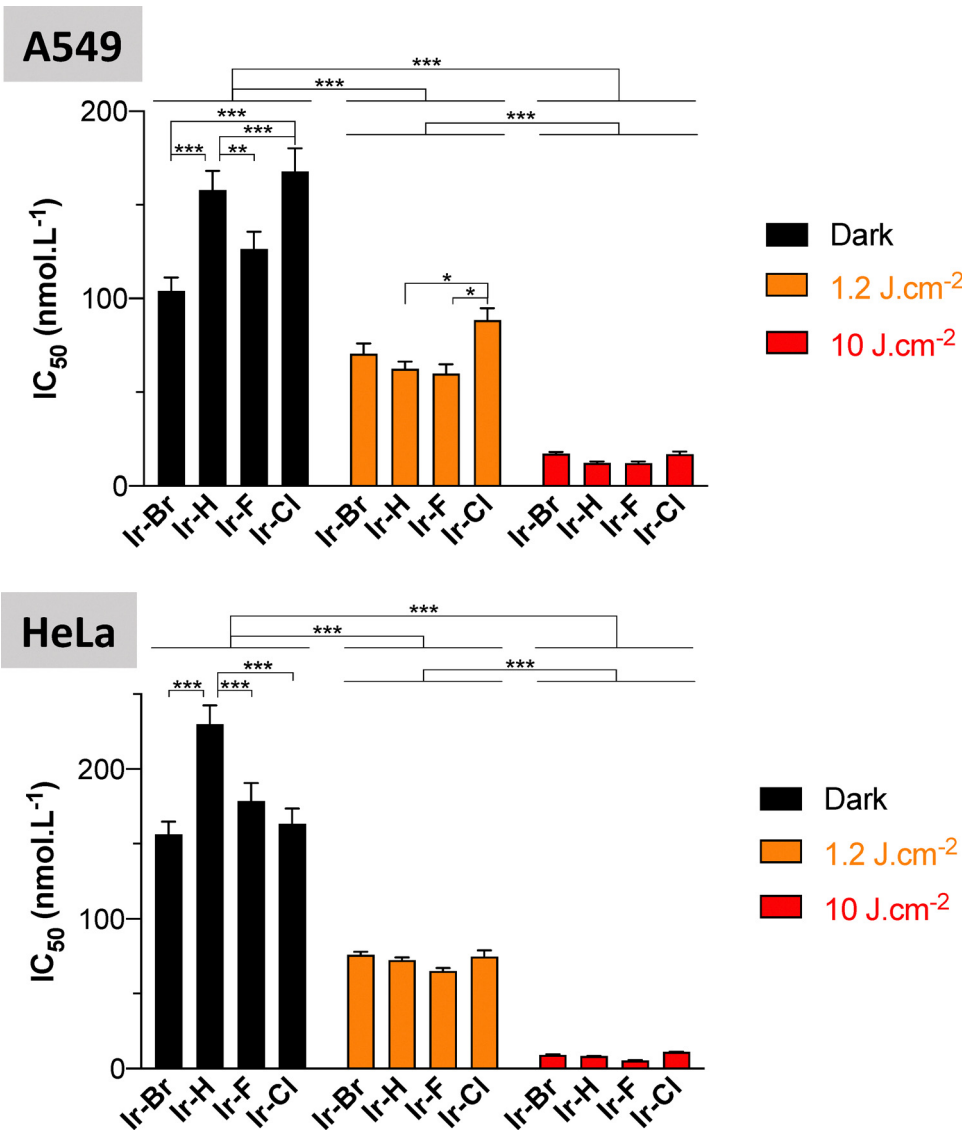

Fig. 6 Concentrations of Ir(III) complexes required to inhibit cell growth by 50% (IC_{50}) after 4 h incubation in A549 or HeLa cells in dark or after light exposure (420 nm; 1.2 and 10 J cm^{-2}). Data represent the mean ± SEM of 4 independent experiments, each performed in triplicate. ** $p < 0.01$; *** $p < 0.001$; two-way ANOVA with Tukey's *post hoc* tests.

phototoxicity.[55] A549 and HeLa cancer cells were subjected to increasing concentrations of **Ir-Br**, **Ir-H**, **Ir-F**, or **Ir-Cl**, and either maintained in the dark or exposed to light 4 h after incubation (Fig. S23). Cyclometallated Ir(III) complexes showed slightly higher dark toxicity in A549 cells compared to HeLa cells, with IC_{50} in the range of 104–168 nM and 156–230 nM respectively (Table 3, Fig. 6). **Ir-H** and **Ir-Cl** were less toxic than **Ir-Br** and **Ir-F** in A549 cells in the dark, while **Ir-H** was the least toxic complex

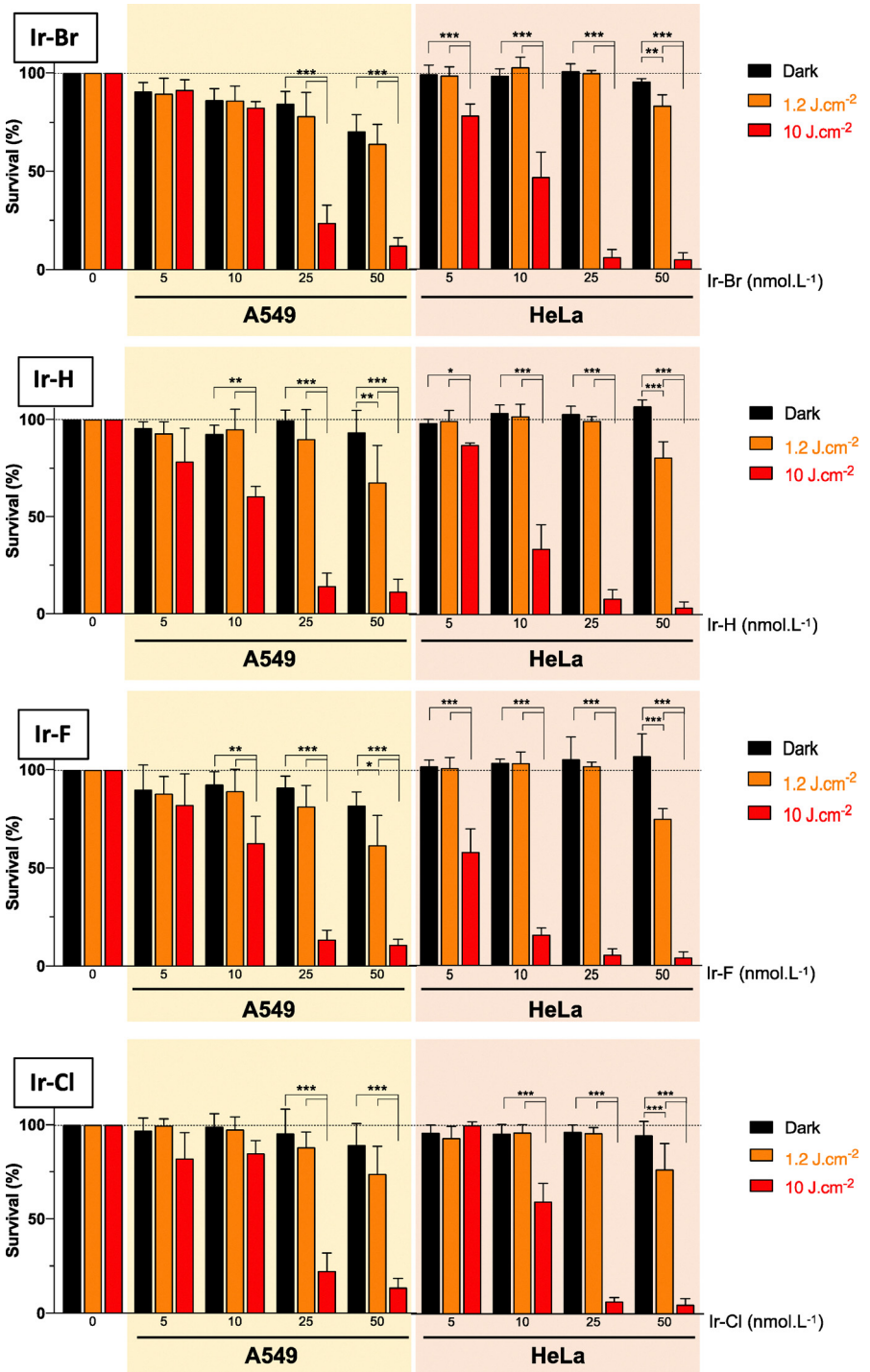

Fig. 7 Cyclometallated Ir(III) complexes induced phototoxicity in A549 and HeLa cells, in a concentration and light-dose dependence manner. A549 and HeLa cells were treated with increasing concentrations of **Ir-H**, **Ir-F**, **Ir-Br** or **Ir-Cl** for 4 h before light exposure at 420 nm (1.2 J cm^{-2} in yellow, and 10 J cm^{-2} in red). Control groups that were not illuminated (shown in black) were kept in the dark. Cell viability was assessed 72 h following light exposure. Data are expressed as the mean ± SEM of 3 independent experiments in triplicate. *$p < 0.05$; **$p < 0.01$; ***$p < 0.001$; ANOVA with Tukey's *post hoc* tests.

in HeLa cells (Table 3 and Fig. 6). It is worth noting that a similar complex with a 2-(pyridinyl)-1-*H*-benzimidazole ancillary ligand instead of 1-butyl-5-methyl-2-(pyridinyl)-1-*H*-benzimidazole used for **Ir-H**, displays lower dark toxicity on A549, and HeLa cells.[56]

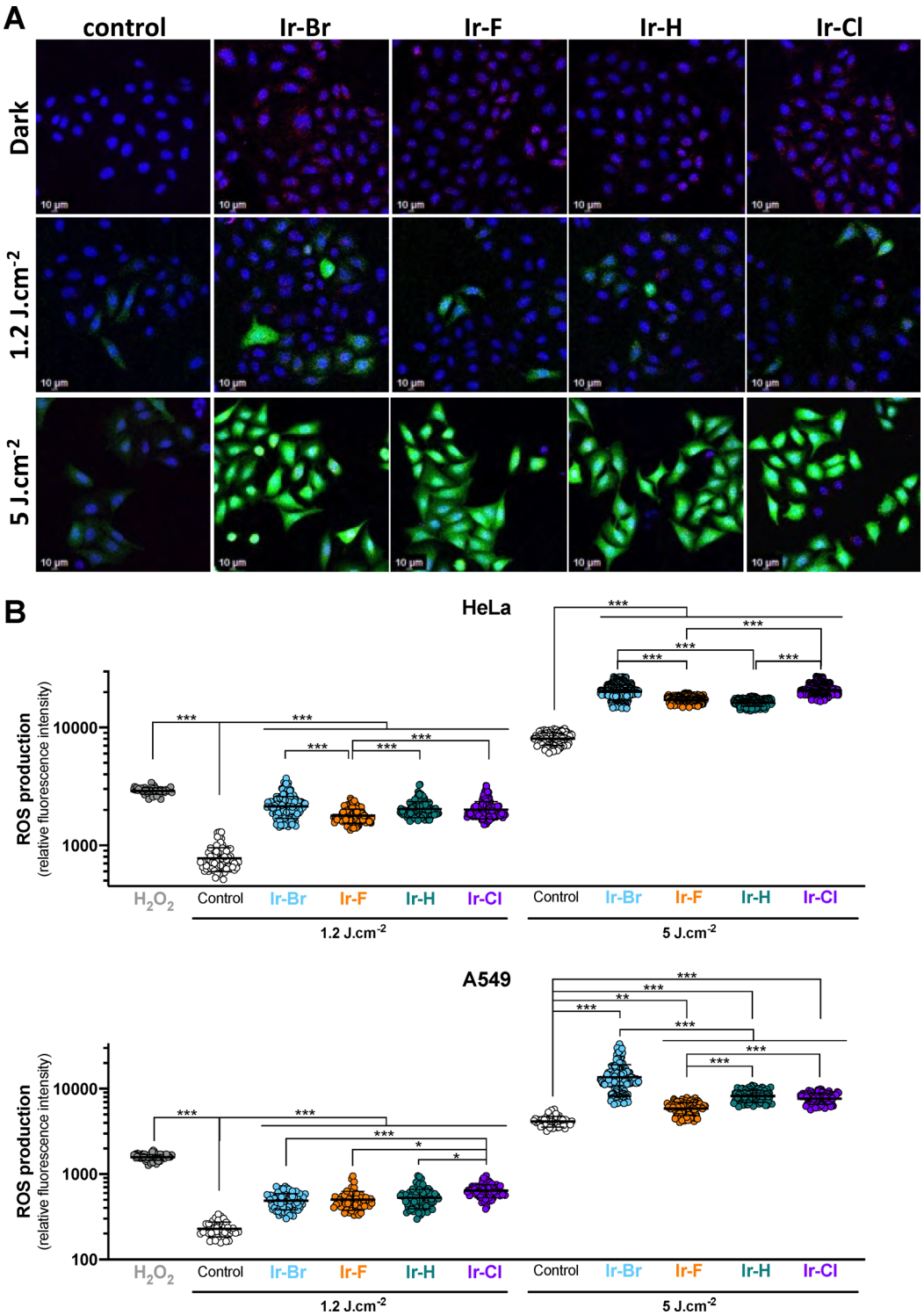

Fig. 8 Cyclometallated Ir(III) complexes generate cellular ROS in A549 and HeLa cells after light exposure. HeLa and A549 cells were incubated with 100 nmol L^{-1} **Ir-H**, **Ir-F**, **Ir-Br** or **Ir-Cl** for 4 h before light exposure at 420 nm (fluency 1.2 and 5 J cm^{-2}) and intracellular ROS detection by DCFH-DA. (A) Confocal images of HeLa cells. **Ir-H**, **Ir-F**, **Ir-Br** or **Ir-Cl** (in red), intracellular ROS detection by DCFH-DA (in green). Nuclei are stained with Hoechst 33342 (in blue). Scale bar = 10 µm. Images are representative of 2 independent experiments. (B) Quantification of ROS production in HeLa and A549 cells. Each dot represents the mean emission intensity of the DCFH-DA dye in a single cell. Bars: mean ± SD (n = 2 independent experiments, performed in duplicates). 100 µmol L^{-1} hydrogen peroxide is used as positive control.

Concentrations of cyclometallated Ir(III) complexes required to inhibit cell growth by 50% (IC_{50}) after 4 h incubation in A549 or HeLa cells in dark or after light exposure (420 nm; 1.2 and 10 J cm^{-2}). Data are expressed as the mean ± SEM of 4 independent experiments performed in triplicate.

All four **Ir-X** complexes exhibited significant phototoxicity, reducing cell viability in both A549 and HeLa cancer cells, compared to their effects in the dark (Fig. S23, Table 3 and Fig. 6). Interestingly, all four complexes induced similar dose-dependent phototoxicity, with IC_{50} in the same range (60–80 nmol L^{-1}) (Table 3 and Fig. 6). It is worth noting that a complex similar to **Ir-H**, with 2-(2-pyridyl)benzimidazole ancillary ligand, displayed a phototoxicity of 1.39 ± 0.05 μmol L^{-1} and 0.95 ± 0.04 nmol L^{-1} for HeLa and A549 respectively under almost identical irradiation fluence at 425 nm (LED light array with 1.2 J cm^{-2}, 4 mW cm^{-2}, 300 s).[56] The complex was localized in the lysosomes while the current **Ir-X** series is localized in the mitochondria, with higher phototoxicity. This could be explained by our ligand design which increases the lipophilicity of the cations with the presence of both the alkyl chain and the halogen atom. Indeed, lipophilic cations are prone to target mitochondria and halogen atoms are also lipophilic substituents.[57] Finaly, it should be noted that **Ir-Cl** appeared to be slightly less potent in reducing the viability of A549 cells than the other complexes at low fluence (1.2 J cm^{-2}), which could be correlated with its Φ_Δ, being the lowest of the series of four complexes.

A minimum concentration of 50 nmol L^{-1} was required for all four complexes to induce significant phototoxicity in HeLa cells at low fluence (1.2 J cm^{-2}) (Fig. 7). However, at this same concentration, only **Ir-H** and **Ir-F** induced significant phototoxicity in A549 cells. At higher fluence (10 J cm^{-2}), significant phototoxicity was induced dose-dependently from 5 nmol L^{-1} **Ir-Br**, **Ir-H**, or **Ir-F**, and from 10 nmol L^{-1} **Ir-Cl** in HeLa cells. Similarly, significant phototoxicity was induced from 10 nmol L^{-1} **Ir-H**, or **Ir-F**, and from 25 nmol L^{-1} **Ir-Br**, or **Ir-Cl** in A549 cells. These data suggest that **Ir-H** and **Ir-F** are slightly more effective at inducing phototoxicity than **Ir-Br** and **Ir-Cl**, which is consistent with their ability to generate singlet oxygen more efficiently and to be better up-taken in cells. Indeed, **Ir-H** and **Ir-F** display the highest Φ_Δ of the series, which is in favor of type II mechanism for the PDT rather than type I.

We next assessed the generation of intracellular reactive oxygen species (ROS) by the four **Ir-X** complexes in A549 and HeLa cells using the widely adopted nonspecific ROS probe, 2′,7′-dichlorodihydrofluorescein diacetate (DCFH-DA). As shown in Fig. 8A, following incubation with all four complexes, HeLa cells displayed green fluorescence signal when exposed to light (420 nm), whereas only weak green fluorescence signal was observed in the control cells. The cellular fluorescence signal of DCFH-DA is strongly enhanced after illumination in HeLa and A549 cells, in a dose-dependent manner (Fig. 8B and Fig. S24). Small variations in the level of ROS production were observed between compounds and cells, and as a function of the fluence used. In particular, **Ir-Br** and **Ir-Cl** appeared to produce slightly more ROS than **Ir-F** and **Ir-H** after 5 J cm^{-2} light exposure in HeLa cells. Similarly, **Ir-Br** produced slightly more ROS than **Ir-F** after exposure in A549 cells that received 5 J cm^{-2}.

Conclusions

A series of four cationic cyclometallated iridium(III) complexes bearing a halogen-substituted 2-pyridylbenzimidazole ancillary ligand (**Ir-X**, X = H, F, Cl, Br), has been designed to enhance photophysical properties for photodynamic therapy (PDT). The incorporation of halogen atoms at the 5′ position of the pyridyl ring effectively modulates the electronic structure, particularly stabilizing the LUMO and narrowing the bandgap, as confirmed by TD-DFT simulations. All complexes exhibit absorption in the visible region, efficient two-photon absorption with a maximum around 700 nm, and high singlet oxygen quantum yields (up to 87%), with **Ir-F** and **Ir-H** outperforming others. Cellular studies in A549 and HeLa cancer cell lines revealed mitochondrial localization, active internalization, and significant light-induced cytotoxicity at nanomolar concentrations (IC_{50} as low as 59.9 nM under 1.2 J cm^{-2}). The complexes also generate both singlet oxygen and superoxide radical upon irradiation, supporting a dual ROS-mediated mechanism. These findings highlight the potential of halogen tuning in optimizing iridium-based photosensitizers for PDT. Among the studied complexes, **Ir-F** and **Ir-H** show promising photophysical and biological properties, suggesting their suitability as theranostic agents for image-guided PDT.

Experimental section

Experimental

Commercially available reagents were purchased from Sigma-Aldrich, Alfa Aesar, Acros Organics, TCI Chemical, Merck, Strem or Fluorochem and used as received unless otherwise specified. Solvents were obtained from the same commercial sources and used without further purification. For moisture sensitive reactions, glassware was oven-dried prior to use. ^{1}H NMR spectra were recorded on a Brucker advance III 400 MHz spectrometer equipped with a BBO probe and on a Brucker advance III 500 MHz spectrometer equipped with a CryoProbe Prodigy in deuterated solvent ($CDCl_3$, DMSO-d_6 or CD_2Cl_2) and data are reported as follows: chemical shift in ppm from tetramethylsilane with the solvent as an internal indicator ($CDCl_3$ 7.26 ppm, DMSO-d_6 2.50 ppm, CD_2Cl_2 5.32 ppm), multiplicity (s = singlet, d = doublet, t = triplet, q = quartet, p = pentet, m = multiplet or overlap of non-equivalent resonances), integration. $^{13}C\{^1H\}$ NMR spectra were recorded either at 101 MHz or at 126 MHz in suitable deuterated solvent and data are reported as follows: chemical shift in ppm from tetramethylsilane with the solvent as an internal indicator ($CDCl_3$ 77.16 ppm, DMSO-d_6 39.52 ppm, CD_2Cl_2 53.84 ppm). ^{19}F NMR spectra were recorded at 376 MHz and at 470 MHz in the suitable deuterated solvent. The synthesis of compounds **2d** and **Ir-Br** have been described elsewhere.[58]

Compound 1 *N*-butyl-3-aminobenzidine

In a round-bottom flask, DMSO was added to a mixture of 4-fluoro-3-nitrotoluene (2 g, 12.9 mmol) and *n*-butylamine (3.4 mL, 34.8 mmol). The flask was sealed with a rubber stopper, and the mixture was heated at 60 °C overnight. The colour of the mixture rapidly changed from yellow to orange. At room temperature, 30 mL of ethylacetate was added to the orange solution, and the organic phase was extracted three times with water and washed with brine. The organic layer was dried over $MgSO_4$, and the product was isolated as a light orange translucent solid (2.2 g, 88%). The product was used without further purification.

^{1}H NMR (400 MHz, $CDCl_3$) δ 8.04 (d, J = 8.8 Hz, 2H), 6.61 (d, J = 1.8 Hz, 2H), 6.43 (dd, J = 8.8, 1.9 Hz, 2H), 3.28 (t, J = 7.1 Hz, 2H), 2.33 (s, 3H), 1.71 (p, J = 7.3 Hz, 2H), 1.48 (h, J = 14.6 Hz, 2H), 0.98 (t, J = 7.3 Hz, 3H). ^{13}C NMR (101 MHz, $CDCl_3$) δ 147.8, 145.8, 130.0, 126.9, 117.0, 113.5, 42.8, 31.1, 22.3, 20.4, 13.9. Elemental analysis for $[C_{11}H_{16}N_2O_2(H_2O)_{0.2}]$, calcd, C, 62.36%; H, 7.80%; N, 13.22%; found C, 62.64%; H, 7.52%; N, 13.23%

General procedure for the pyridylbenzimidazole derivatives

In a round bottom flask, a mixture of methoxyethanol/water or DMF/water (5 : 2) was added on compound **1** (1 eq.) and suitable 2-pyridinecarboxaldehyde (1 eq.). When solids were dissolved, $Na_2S_2O_4$ (9.2 eq.) was added, and the solution was heated at 100 °C overnight. At r.t., water (30 mL) was added, followed by 30 mL of ethylacetate. The phases were separated, and the organic layer was washed 3× with water, once with brine, and finally dried over Na_2SO_4. The pure compound was obtained after removing the solvents under vacuum. In some case, further purification was needed and consisted in a flash chromatography (SiO_2).

Compound **2a** 1-*n*-butyl-5-methyl-2-(pyridin-2-yl)-1-benzimidazole: **1** (400 mg, 1.92 mmol) and 2-pyridinecarboxaldehyde (200 mg, 1.92 mmol) and $Na_2S_2O_4$ (3.36 g, 17.7 mmol) in DMF/water (14 mL). After solvent evaporation, the compound was obtained as a light beige solid (475 mg, 89%) and used without further purification. ^{1}H NMR (400 MHz, $CDCl_3$) δ 8.68 (d, J = 4.9 Hz, 1H), 8.44 (d, J = 8.0 Hz, 1H), 7.84 (dd, J = 7.8 Hz, J = 1.8 Hz, 1H), 7.74 (d, J = 8.3 Hz, 1H), 7.33 (ddd, J = 7.6 Hz, J = 4.8 Hz, J = 1.2 Hz, 1H), 7.24 (s, 1H), 7.15 (dd, J = 8.2 Hz, J = 1.6 Hz, 1H), 4.82 (t, J = 7.3 Hz, 2H), 2.54 (s, 3H), 1.92–1.80 (m, 2H), 1.45–1.31 (m, 2H), 0.93 (t, J = 7.4 Hz, 3H). ^{13}C NMR (101 MHz, $CDCl_3$) δ 148.7, 136.9, 124.9, 124.6, 123.8, 119.5, 110.2, 45.4, 32.3, 27.1, 20.2, 13.9. HRMS calcd for [M + H] 266.1657, found 266.16499.

Compound **2b** 1-*n*-butyl-5-methyl-2-(5-fluoropyridin-2-yl)-1-benzimidazole: **1** (400 mg, 1.92 mmol) and suitable 5-fluoro-2-pyridinecarboxaldehyde (240 mg, 1.92 mmol) and $Na_2S_2O_4$ (3.36 g, 17.7 mmol). After solvent evaporation, the crude compound was purified by flash chromatography column (SiO_2, cyclohexane/ethylacetate, 4/1). **2b** was obtained as a light beige solid (108 mg, 20%). ^{1}H NMR (400 MHz, $CDCl_3$) δ 8.53 (d, J = 2.9 Hz, 1H), 8.44 (ddd, J = 8.9, 4.5, 0.6 Hz, 1H), 7.65 (d, J = 8.2 Hz, 1H), 7.55 (ddd, J = 8.6, 8.6, 3.0 Hz, 1H), 7.26 (s, 1H), 7.13 (dd, J = 8.3, 1.6 Hz, 1H), 4.74 (t, J = 7.7 Hz, 2H), 2.54 (s, 3H), 1.91–1.79 (m, 2H), 1.47–1.33 (m, 3H), 0.96 (t, J = 7.4 Hz, 3H). ^{19}F NMR (376 MHz, CD_2Cl_2) δ −126.99. ^{13}C NMR (101 MHz, $CDCl_3$) ^{13}C NMR (101 MHz, $CDCl_3$) δ 148.8, 147.4, 140.9, 137.0, 136.9, 136.7, 133.5, 126.2, 126.1, 124.5, 124.0, 123.8, 119.7, 110.2, 45.3, 32.3, 22.2, 20.3, 13.9. HRMS calcd for [M + H] 284.1563, found 284.15536.

Compound **2c** 1-*n*-butyl-5-methyl-2-(5-chloropyridin-2-yl)-1-benzimidazole: **1** (400 mg, 1.92 mmol) and 5-chloro-2-pyridinecarboxaldehyde (240 mg, 1.92 mmol) and $Na_2S_2O_4$ (3.36 g, 17.7 mmol). After solvent evaporation, the crude compound was purified by flash chromatography column (SiO_2, cyclohexane/ethylacetate, 3/2). **2c** was obtained as a light beige solid (267 mg, 47%). ^{1}H NMR (400 MHz, $CDCl_3$) 8.63 (d, J = 2.2 Hz, 1H), 8.46 (d, J = 8.5 Hz, 1H), 7.82 (dd, J = 8.6, 2.5 Hz, 1H), 7.73 (d, J = 8.3 Hz, 1H), 7.23 (s, 1H), 7.16 (d, J = 8.3 Hz, 1H), 4.78 (t, J = 7.6 Hz, 2H), 2.54 (s, 3H), 1.91–1.79 (m, 2H), 1.46–1.31 (m, 2H), 0.95 (t, J = 7.4 Hz, 3H). ^{13}C NMR (101 MHz, $CDCl_3$) δ 147.7, 136.9, 125.8, 215.1, 110.3, 45.6, 32.3, 22.2, 20.2, 13.9. HRMS calcd for [M + H] 300.1268, found 300.12568.

General procedure for the Ir-X complexes

In a round bottom flask, a mixture of CH_2Cl_2/MeOH (1 : 1) was added on compound **2** (2 eq.) and di-μ-chloridotetrakis[2-pyridylphenyl]diiridium(III) ($[[(N^C)_2Ir)_2Cl_2]$, 1 eq.) and the solution was refluxed overnight. At r.t., the solution was concentrated to the 2/3 and a saturated solution of aqueous $NaPF_6$ was added dropwise until the apparition of a persistent precipitate. The suspension was filtrated with a Millipore® and washed with small portion of water, ice-cold methanol and diethylether. The resulting solid was dissolved in CH_2Cl_2, filtrated on Célite® and recrystallized by slow vapour diffusion of pentane. The supernatant was removed (Millipore®) and the solid was dried under vacuum.

Ir-H. 2a (70 mg, 0.26 mmol), $[[(N^C)_2Ir)_2Cl_2]$ 140 mg (0.13 mmol) and solvents (20 mL). The compound was obtained as a yellow solid (146 mg, 56%). ^{1}H NMR (500 MHz, CD_2Cl_2) δ 8.34 (d, J = 8.2 Hz, 1H), 8.20 (td, J = 8.0 Hz, J = 1.7 Hz, 1H), 8.10 (ddd, J = 5.5 Hz, J = 1.7 Hz, J = 0.7 Hz, 1H), 7.99–7.93 (m, 1H), 7.89 (d, J = 8.1 Hz, 1H), 7.81–7.69 (m, 4H), 7.63 (ddd, J = 5.8 Hz, J = 1.6 Hz, J = 0.8 Hz, 1H), 7.48 (ddd, J = 5.8 Hz, J = 1.5 Hz, J = 0.8 Hz, 1H), 7.44 (ddd, J = 7.7 Hz, J = 5.4 Hz, J = 1.1 Hz, 1H), 7.36 (s, 1H), 7.10 (dtd, J = 14.0 Hz, J = 7.5 Hz, J = 1.2 Hz, 2H), 7.01–6.86 (m, 5H), 6.41 (dd, J = 7.6 Hz, J = 1.2 Hz, 1H), 6.34 (dd, J = 7.6 Hz, J = 1.2 Hz, 1H), 6.24 (d, J = 8.5 Hz, 1H), 4.81–4.68 (m, 2H), 2.45 (s, 3H), 2.07–1.93 (m, 2H), 1.50 (q, J = 7.6 Hz, 2H), 1.01 (t, J = 7.3 Hz, 3H). ^{13}C NMR (126 MHz, CD_2Cl_2) δ 168.3, 168.2, 152.7, 151.6, 151.3, 149.7, 148.9, 147.6, 147.6, 144.6, 144.4, 140.1, 138.4, 138.2, 138.1, 137.7, 137.2, 132.7, 131.9, 131.1, 130.4, 128.2, 127.7, 125.3, 125.0, 124.9, 123.6, 123.5, 123.0, 122.8, 120.1, 119.8, 118.3, 111.3, 46.3, 32.2, 22.1, 20.4, 13.9. HRMS calcd for $[M^+]$ 766.2516, found 766.25131.

Ir-F. 2b (60 mg, 0.21 mmol), $[[(N^C)_2Ir)_2Cl_2]$ (100 mg, 0.09 mmol) and solvents (20 mL). The compound was obtained as a bright yellow solid (175 mg, 90%). ^{1}H NMR (500 MHz,

CD_2Cl_2) δ 8.42 (dd, J = 9.1, 4.5 Hz, 1H), 8.06–7.95 (m, 2H), 7.92 (t, J = 2.3 Hz, 1H), 7.89 (d, J = 8.1 Hz, 1H), 7.84–7.70 (m, 4H), 7.64 (ddd, J = 5.9, 1.6, 0.8 Hz, 1H), 7.51 (ddd, J = 5.8, 1.6, 0.8 Hz, 1H), 7.35 (s, 1H), 7.11 (qd, J = 7.5, 1.2 Hz, 2H), 7.01 (ddd, J = 7.3, 5.8, 1.4 Hz, 1H), 7.00–6.90 (m, 3H), 6.88 (dd, J = 8.6, 1.5 Hz, 1H), 6.39 (dd, J = 7.6, 1.2 Hz, 1H), 6.33 (dd, J = 7.6, 1.2 Hz, 1H), 6.23 (d, J = 8.5 Hz, 1H), 4.81–4.67 (m, 2H), 2.45 (s, 3H), 2.05–1.91 (m, 2H), 1.54–1.43 (m, 2H), 1.00 (t, J = 7.3 Hz, 3H). ^{3}C{H} NMR (126 MHz, CD_2Cl_2) δ 167.7, 162.0, 159.9, 150.6, 150.2, 149.4, 148.6, 146.3, 144.1, 144.0, 141.4, 141.1, 138.1, 137.9, 137.6, 137.2, 136.7, 132.1, 131.6, 130.9, 130.0, 127.3, 126.9, 126.8, 126.2, 125.0, 124.6, 123.4, 123.2, 122.9, 122.5, 119.8, 119.4, 117.8, 111.0, 45.8, 31.8, 21.7, 20.0, 13.5. ^{19}F NMR (470 MHz, CD_2Cl_2) δ −72.36, −73.87, −116.82. HRMS calcd for [M^+] 784.2427, found 784.24110.

Ir-Cl. 2c (100 mg, 0.34 mmol), [((N^C)$_2$Ir)$_2$Cl$_2$] (180 mg, 0.17 mmol) and solvents (20 mL). The compound was obtained as a yellow solid (172 mg, 51%). ^{1}H NMR (500 MHz, CD_2Cl_2) δ 8.35 (d, J = 8.8 Hz, 1H), 8.20 (dd, J = 8.8 Hz, J = 2.4 Hz, 1H), 8.01–7.95 (m, 2H), 7.89 (dd, J = 8.2 Hz, J = 1.1 Hz, 1H), 7.84–7.75 (m, 2H), 7.75–7.71 (m, 2H), 7.63 (dt, J = 5.7 Hz, J = 1.3 Hz, 1H), 7.53 (dt, J = 5.8 Hz, J = 1.0 Hz, 1H), 7.36 (s, 1H), 7.11 (tdd, J = 7.3 Hz, J =5.7 Hz, J = 1.2 Hz, 2H), 7.02 (ddd, J = 7.4 Hz, J = 5.8 Hz, J = 1.5 Hz, 1H), 6.99–6.92 (m, 3H), 6.89 (dd, J = 8.6 Hz, J = 1.6 Hz, 1H), 6.38 (dd, J = 7.6 Hz, J = 1.2 Hz, 1H), 6.33 (dd, J = 7.5 Hz, J = 1.2 Hz, 1H), 6.24 (d, J = 8.5 Hz, 1H), 4.82–4.68 (m, 2H), 2.45 (s, 3H), 1.98 (h, J = 7.4 Hz, 2H), 1.47 (h, J = 7.7 Hz, 2H), 0.99 (t, J = 7.3 Hz, 3H). ^{13}C NMR (126 MHz, CD_2Cl_2) δ 168.2, 168.1, 151.3, 151.0, 150.6, 149.8, 149.1, 146.8, 146.0, 144.5, 144.4, 139.9, 138.6, 138.3, 138.1, 137.9, 137.3, 136.3, 132.5, 132.0, 131.3, 130.5, 127.9, 125.5, 125.0, 123.8, 123.7, 123.3, 123.0, 120.3, 119.8, 118.3, 111.4, 46.3, 32.2, 22.1, 20.4, 13.9. HRMS calcd for [M^+] 800.2126, found 800.21146.

EPR experiments

The EPR spectra have been recorded on a Bruker EMS Plus spectrometer equipped with a X-band cavity (9.4 GHz) with irradiation window from 100 K to 370 K. Both **Ir-X** and DMPO were solubilized together in MeOH avoiding light exposure, with concentration of 0.1 mM and 60 mM respectively. A first spectrum was recorded at r.t. in dark. Then, a second spectrum was recorded after 5 min illumination with a blue diode (415 nm).

Cell lines and culture

The human lung adenocarcinoma A549 and cervical cancer HeLa cell lines were obtained from LGC standard (Molsheim, France). All cells were routinely tested for the presence of mycoplasma (Mycoalert® Mycoplasma Detection Kit, Lonza, Rockland, ME, USA) and used within three months after thawing. Cells were maintained in culture at 37 °C in medium with 10% FBS in a 5% CO_2 humidified atmosphere. The cell morphology was routinely checked.

Cellular uptake and subcellular localization

Cells were treated with 1 μmol L^{-1} **Ir-Br**, **Ir-H**, **Ir-F**, or **Ir-Cl** for 4 h at 37 °C or 4 °C, before flow cytometry study (Attune NxT, Thermo Fisher Scientific, New York city, NY, US). Flow cytometry analysis was performed using FCS Express 7 software (*De Novo* Software, Dotmatics, Pasadena, CA, US).

After 4 h treatment with complexes, the cells were stained with 25 nmol L^{-1} MitoTracker Orange and 120 nmol L^{-1} LysoTracker blue (Invitrogen, ThermoFisher Scientific) for 30 min at 37 °C. The cells were then washed with PBS to eliminate any excess dye and examined using a Stellaris confocal microscope equipped with a white laser (Leica Microsystems) and with a 63× objective (HC PL APO CS2, 1.2 water). The fluorescence images from dyes were collected in the range λ_{em} = 410–455 nm (λ_{ex} = 405 nm) for LysoTracker, and in the range λ_{em} = 556–642 nm (λ_{ex} = 551 nm) for MitoTracker. All four complexes were imaged in the range λ_{em} = 670–800 nm (λ_{ex} = 405 nm). Analysis of complexes colocalization with lysosomes and mitochondria was performed using the BIOP_JaCoB plugin in FIJI (Image J version 1.54f, National Institutes of Health, Bethesda, MD, USA). Pearson's correlation coefficient was calculated to assess colocalization.

In vitro cytotoxicity assays

Cell proliferation assays were conducted in 96-well culture plates. Cells were cultured for 24 h prior to treatment with increasing concentration of **Ir-Br**, **Ir-H**, **Ir-F**, or **Ir-Cl** in complete medium. Illumination at 420 nm with power output at 78 mW cm^{-2} (15 s, fluency 1.2 J cm^{-2} and 128 s, fluency 10 J cm^{-2}) (Lumidox® II 96-position LED Array, Analytical Sales and Services, Flanders, US) was performed 4 h after treatment. The cell viability was quantified 72 h after light exposure with the 3-(4,5-dimethylthiazol-2-yl)-2,5-diphenyltetrazolium bromide assay (MTT assay). Cell viability was normalized to control cells (no drug and no illumination). The drug concentrations required to inhibit cell growth by 50% (IC_{50}) were determined by interpolation from the dose to response curves.

ROS generation in cells

A549 and HeLa cells were incubated with 100 nmol L^{-1} **Ir-Br**, **Ir-H**, **Ir-F**, or **Ir-Cl** for 4 h. Twenty-five μmol L^{-1} 2′,7′-dichlorodihydrofluorescein diacetate (H_2DCFH-DA, Sigma-Aldrich, France) were then incubated for 30 min. Hoechst (5 μmol L^{-1}) was used to counterstain the cell nuclei. The fluorescence images before and after 420 nm irradiation (fluency 1.2 J cm^{-2} or 5 J cm^{-2}) were acquired using a Stellaris 8 confocal microscope. A 10× objective (HC PL APO, NA = 0.40) was used to collect the light. The emission from the Hoechst dye was collected in the range λ_{em} = 412–464 nm (HyD detector), upon excitation with the 405 nm laser diode. The four complexes were imaged using the same excitation diode (λ_{ex} = 405 nm) and the emission was collected within the range λ_{em} = 670–800 nm (HyD detector). The emission of the H_2DCFH-DA dye was measured upon excitation at λ_{ex} = 491 nm and the light was collected in the range λ_{em} = 500–547 nm (HyD detector). Image analysis was conducted using the ''Analysis'' module within the LasX software of the Stellaris microscope. Each cell was individually identified, and the mean intensity of emission of the DHF dye was quantified per cell.

Statistical analyses

All analyses were performed using the GraphPad Prism software (GraphPad Software, San Diego, CA). Two-sided p-values <0.05 were considered significant.

Absorption and emission spectroscopies

Absorption spectra were recorded on a Cary 300 UV-visible spectrophotometer (Varian) and emission spectra (in solution and at 77 K) were recorded on a Fluoromax 4® (Horiba) or on a FLS-1000® (Edinburgh Instruments) equipped with automatic filters to remove the harmonic bands. Quartz cuvettes with 1 cm optical path were used. Lifetimes were measured using LP900 spectrometer with a Flashlamp pumped Q-switched Nd:Yag laser operating at 355 nm and with photomulitplier (PMT) detector, or with a picosecond laser diode operating at 405 nm and using a time-correlated single photon counting detection (TCSPC, PicoHarp 300).

Computational details

Density functional theory (DFT) simulations have been performed using the Gaussian16 package.[59] Based on previous theoretical investigations conducted by some of us,[60–63] we considered the B3PW91 functional[64–66] in addition to the Def2TZVP basis set, which includes a pseudopotential to describe core electrons for large atoms together with polarization functions. The polarizable continuum model (PCM)[67,68] was used to take into account solvent effects (CH_2Cl_2). To save on computation, the Me fragments were replaced by hydrogen after careful check of the substitution impact. Geometry relaxations of the singlet (ground state) and triplet (excited state) states were performed and carefully checked by the calculation of the vibrational frequencies. The general Adiabatic Hessian approach (AH)[69] was considered for estimating vibrational contributions into the computation of emission spectra. Post-treatments were done using the Gaussview, in-house python programs and the VMS packages.[70–72]

Author contributions

The manuscript was written through contribution of all authors./All authors have given approval to the final version of the manuscript.

Conflicts of interest

The authors have no conflicts of interest.

Data availability

We confirm that all data generated or analysed during this study are included in the published article. Additional details regarding the methodology and results are provided in the supplementary information (SI) file submitted alongside the manuscript. Supplementary information is available. See DOI: **https://doi.org/10.1039/d5ma00964b**.

C. L. should be contacted for the calculation requests, Camille.Latouche@cnrs-imn.fr.

CCDC 2091730, 2091731, 2091732, 2338300 and 2338301 contain the supplementary crystallographic data for this paper.[73a–e]

Acknowledgements

This work benefited from state aid managed by the National Research Agency under the ''Investments for the future'' and of the ''Investissements d'avenir'' program bearing the reference ANR-15-IDEX-02. This work was partially supported by CBH-EUR-GS (ANR-17-EURE-0003). A.-L. B. acknowledges the support of the European Research Council (ERC STG, RADIANCE, 101116304). Views and opinions expressed are however those of the authors only and do not necessarily reflect those of the European Union or the European Research Council Executive Agency. Neither the European Union nor the granting authority can be held responsible for them. The authors thank the CNRS and Université de Grenoble Alpes for their support. The Nano-Bio ICMG (UAR 2607) is acknowledged for providing facilities for mass spectrometry (A. Durand, L. Fort and R. Gueret), EPR spectrometer, and single crystal X-ray diffraction (N. Altounian). The theoretical investigations were performed using the computing facilities of the CCIPL (Centre de Calculs Intensifs des Pays de la Loire). CL thanks the IUF for supporting his research.

References

1 T.-Y. Li, J. Wu, Z.-G. Wu, Y.-X. Zheng, J.-L. Zuo and Y. Pan, Rational Design of Phosphorescent Iridium(III) Complexes for Emission Color Tunability and Their Applications in OLEDs, *Coord. Chem. Rev.*, 2018, **374**, 55–92, DOI: **10.1016/j.ccr.2018.06.014**.

2 S. B. Meier, D. Tordera, A. Pertegàs, C. Roldàn-Carmona, E. Ortì and H. J. Bolink, Light-Emitting Electrochemical Cells: Recent Progress and Future Prospects, *Mater. Today*, 2014, **17**(5), 217–223, DOI: **10.1016/j.mattod.2014.04.029**.

3 A. Salehi, X. Fu, D.-H. Shin and F. So, Recent Advances in OLED Optical Design, *Adv. Funct. Mater.*, 2019, **29**(15), 1808803, DOI: **10.1002/adfm.201808803**.

4 J. H. Zhao, Y. X. Hu, H. Y. Lu, Y. L. Lü and X. Li, Progress on Benzimidazole-Based Iridium(III) Complexes for Application in Phosphorescent OLEDs, *Org. Electron.*, 2017, **41**, 56–72, DOI: **10.1016/j.orgel.2016.11.039**.

5 K. K.-W. Lo, Luminescent Rhenium(I) and Iridium(III) Polypyridine Complexes as Biological Probes, Imaging Reagents, and Photocytotoxic Agents, *Acc. Chem. Res.*, 2015, **48**(12), 2985–2995, DOI: **10.1021/acs.accounts.5b00211**.

6 Y. J. Yuan, Z. T. Yu, D. Q. Chen and Z. G. Zou, Metal-Complex Chromophores for Solar Hydrogen Generation, *Chem. Soc. Rev.*, 2017, **46**(3), 603–631, DOI: **10.1039/c6cs00436a**.

7 J. H. Shon and T. S. Teets, Molecular Photosensitizers in Energy Research and Catalysis: Design Principles and

Recent Developments, *ACS Energy Lett.*, 2019, **4**(2), 558–566, DOI: 10.1021/acsenergylett.8b02388.

8 A. I. Solomatina, A. D. Slobodina, E. V. Ryabova, O. I. Bolshakova, P. S. Chelushkin, S. V. Sarantseva and S. P. Tunik, Blood-Brain Barrier Penetrating Luminescent Conjugates Based on Cyclometalated Platinum(II) Complexes, *Bioconjugate Chem.*, 2020, **31**(11), 2628–2637, DOI: 10.1021/acs.bioconjchem.0c00542.

9 L. Flamigni, A. Barbieri, C. Sabatini, B. Ventura and F. Barigelletti, Photochemistry and Photophysics of Coordination Compounds: Iridium, *Photochemistry and Photophysics of Coordination Compounds II*, 2007, pp. 143–203.

10 J.-H. Shon, S. Sittel and T. S. Teets, Synthesis and Characterization of Strong Cyclometalated Iridium Photoreductants for Application in Photocatalytic Aryl Bromide Hydrodebromination, *ACS Catal.*, 2019, **9**(9), 8646–8658, DOI: 10.1021/acscatal.9b02759.

11 H. Na and T. S. Teets, Highly Luminescent Cyclometalated Iridium Complexes Generated by Nucleophilic Addition to Coordinated Isocyanides, *J. Am. Chem. Soc.*, 2018, **140**(20), 6353–6360, DOI: 10.1021/jacs.8b02416.

12 P.-H. Lanoë, C. M. Tong, R. W. Harrington, M. R. Probert, W. Clegg, J. A. G. Williams and V. N. Kozhevnikov, Ditopic Bis-Terdentate Cyclometallating Ligands and Their Highly Luminescent Dinuclear Iridium(III) Complexes, *Chem. Commun.*, 2014, **50**(52), 6831–6936, DOI: 10.1039/c4cc01808g.

13 H. Sasabe, J. Takamatsu, T. Motoyama, S. Watanabe, G. Wagenblast, N. Langer, O. Molt, E. Fuchs, C. Lennartz and J. Kido, High-Efficiency Blue and White Organic Light-Emitting Devices Incorporating a Blue Iridium Carbene Complex, *Adv. Mater.*, 2010, **22**(44), 5003–5007, DOI: 10.1002/adma.201002254.

14 D. G. Congrave, Y.-T. Hsu, A. S. Batsanov, A. Beeby and M. R. Bryce, Sky-Blue Emitting Bridged Diiridium Complexes: Beneficial Effects of Intramolecular π–π Stacking, *Dalton Trans.*, 2018, **47**(47), 2086–2098, DOI: 10.1039/C7DT04201A.

15 X. Wang, S. Wang, F. Pan, L. He and L. Duan, Cationic Iridium Complexes with 5-Phenyl-1*H*-1,2,4-Triazole Type Cyclometalating Ligands: Toward Blue-Shifted Emission, *Inorg. Chem.*, 2019, **58**(18), 12132–12145, DOI: 10.1021/acs.inorgchem.9b01433.

16 A. F. Henwood, A. K. Pal, D. B. Cordes, A. M. Z. Slawin, T. W. Rees, C. Momblona, A. Babaei, A. Pertegás, E. Ortí, H. J. Bolink, E. Baranoff and E. Zysman-Colman, Blue-Emitting Cationic Iridium(III) Complexes Featuring Pyridylpyrimidine Ligands and Their Use in Sky-Blue Electroluminescent Devices, *J. Mater. Chem. C*, 2017, **5**(37), 9638–9650, DOI: 10.1039/c7tc03110f.

17 L. He, Y. Lan, D. Ma, X. Song and L. Duan, Fluorine-Free, Highly Efficient, Blue-Green and Sky-Blue-Emitting Cationic Iridium Complexes and Their Use for Efficient Organic Light-Emitting Diodes, *J. Mater. Chem. C*, 2018, **6**(6), 1509–1520, DOI: 10.1039/c7tc04747a.

18 V. N. Kozhevnikov, Y. Zheng, M. Clough, H. A. Al-Attar, G. C. Griffiths, K. Abdullah, S. Raisys, V. Jankus, M. R. Bryce and A. P. Monkman, Cyclometalated Ir(III) Complexes for High-Efficiency Solution-Processable Blue PhOLEDs, *Chem. Mater.*, 2013, **25**(11), 2352–2358, DOI: 10.1021/cm4010773.

19 C. Caporale and M. Massi, Cyclometalated Iridium(III) Complexes for Life Science, *Coord. Chem. Rev.*, 2018, **363**, 71–91, DOI: 10.1016/j.ccr.2018.02.006.

20 L. K. McKenzie, H. E. Bryant and J. A. Weinstein, Transition Metal Complexes as Photosensitisers in One- and Two-Photon Photodynamic Therapy, *Coord. Chem. Rev.*, 2019, **379**, 2–29, DOI: 10.1016/j.ccr.2018.03.020.

21 A. F. Henwood and E. Zysman-Colman, Luminescent Iridium Complexes Used in Light-Emitting Electrochemical Cells (LEECs), *Top. Curr. Chem.*, 2016, **374**, 36, DOI: 10.1007/s41061-016-0036-0.

22 C. E. Housecroft and E. C. Constable, Over the LEC Rainbow: Colour and Stability Tuning of Cyclometallated Iridium(III) Complexes in Light-Emitting Electrochemical Cells, *Coord. Chem. Rev.*, 2017, **350**, 155–177, DOI: 10.1016/j.ccr.2017.06.016.

23 D. Rota Martir and E. Zysman-Colman, Supramolecular Iridium(III) Assemblies, *Coord. Chem. Rev.*, 2018, **364**, 86–117, DOI: 10.1016/j.ccr.2018.03.016.

24 R. D. Costa, E. Ortí, H. J. Bolink, S. Graber, S. Schaffner, M. Neuburger, C. E. Housecroft and E. C. Constable, Archetype Cationic Iridium Complexes and Their Use in Solid-State Light-Emitting Electrochemical Cells, *Adv. Funct. Mater.*, 2009, **19**(21), 3456–3463, DOI: 10.1002/adfm.200900911.

25 K. P. S. Zanoni, R. L. Coppo, R. C. Amaral and N. Y. Murakami Iha, Ir(III) Complexes Designed for Light-Emitting Devices: Beyond the Luminescence Color Array, *Dalton Trans.*, 2015, **44**(33), 14559–14573, DOI: 10.1039/c5dt01644d.

26 S. S. Kelkar and T. M. Reineke, Theranostics: Combining Imaging and Therapy, *Bioconjugate Chem.*, 2011, **22**(10), 1879–1903, DOI: 10.1021/bc200151q.

27 T. Nagaya, Y. A. Nakamura, P. L. Choyke and H. Kobayashi, Fluorescence-Guided Surgery, *Front. Oncol.*, 2017, **7**, 314, DOI: 10.3389/fonc.2017.00314.

28 C. Zhang, K. Qiu, C. Liu, H. Huang, T. W. Rees, L. Ji, Q. Zhang and H. Chao, Tracking Mitochondrial Dynamics during Apoptosis with Phosphorescent Fluorinated Iridium(III) Complexes, *Dalton Trans.*, 2018, **47**(37), 12907–12913, DOI: 10.1039/c8dt02918k.

29 S. Shaikh, Y. Wang, F. ur Rehman, H. Jiang and X. Wang, Phosphorescent Ir(III) Complexes as Cellular Staining Agents for Biomedical Molecular Imaging, *Coord. Chem. Rev.*, 2020, **416**, 213344, DOI: 10.1016/j.ccr.2020.213344.

30 D. E. J. G. J. Dolmans, D. Fukumura and R. K. Jain, Photodynamic Therapy for Cancer, *Nat. Rev. Cancer*, 2003, **3**(5), 380–387.

31 L. Li, L. Zhang, X. Tong, Y. Li, Z. Yang, D. Zhu, Z. Su and Z. Xie, Near-Infrared-Emitting AIE Multinuclear Cationic Ir(III) Complex-Assembled Nanoparticles for Photodynamic Therapy, *Dalton Trans.*, 2020, **49**(43), 15332–15338, DOI: 10.1039/d0dt02962a.

32 L. Zhang, Y. Li, W. Che, D. Zhu, G. Li, Z. Xie, N. Song, S. Liu, B. Z. Tang, X. Liu, Z. Su and M. R. Bryce, AIE Multinuclear Ir(III) Complexes for Biocompatible Organic Nanoparticles with Highly Enhanced Photodynamic Performance, *Adv. Sci.*, 2019, **6**(5), 1–7, DOI: **10.1002/advs.201802050**.

33 Y. Xu, X. Wang, K. Song, J. Du, J. Liu, Y. Miao and Y. Li, BSA-Encapsulated Cyclometalated Iridium Complexes as Nano-Photosensitizers for Photodynamic Therapy of Tumor Cells, *RSC Adv.*, 2021, **11**(25), 15323–15331, DOI: **10.1039/d1ra01740c**.

34 X. Cai, K. N. Wang, W. Ma, Y. Yang, G. Chen, H. Fu, C. Cui, Z. Yu and X. Wang, Multifunctional AIE Iridium(III) Photosensitizer Nanoparticles for Two-Photon-Activated Imaging and Mitochondria Targeting Photodynamic Therapy, *J. Nanobiotechnol.*, 2021, **19**(1), 1–13, DOI: **10.1186/s12951-021-01001-4**.

35 Z. Wang, L. Li, W. Wang, R. Wang, G. Li, H. Bian, D. Zhu and M. R. Bryce, Self-Assembled Nanoparticles Based on Cationic Mono-/AIE Tetra-Nuclear Ir(III) Complexes: Long Wavelength Absorption/near-Infrared Emission Photosensitizers for Photodynamic Therapy, *Dalton Trans.*, 2023, **52**(6), 1595–1601, DOI: **10.1039/d2dt03809a**.

36 S. Liu, J. Han, W. Wang, Y. Chang, R. Wang, Z. Wang, G. Li, D. Zhu and M. R. Bryce, AIE-Active Ir(III) Complexes Functionalised with a Cationic Schiff Base Ligand: Synthesis, Photophysical Properties and Applications in Photodynamic Therapy, *Dalton Trans.*, 2022, **51**(42), 16119–16125, DOI: **10.1039/d2dt02960j**.

37 S. Pascal, S. David, C. Andraud and O. Maury, Near-Infrared Dyes for Two-Photon Absorption in the Short-Wavelength Infrared: Strategies towards Optical Power Limiting, *Chem. Soc. Rev.*, 2021, **50**(11), 6613–6658, DOI: **10.1039/d0cs01221a**.

38 E. Martìnez-Vollbert, C. Ciambrone, W. Lafargue-Dit-Hauret, C. Latouche, F. Loiseau and P.-H. Lanoë, Bis-Heteroleptic Cationic Iridium(III) Complexes Featuring Cyclometalating 2-Phenylbenzimidazole Ligands: A Combined Experimental and Theoretical Study, *Inorg. Chem.*, 2022, **61**(61), 3033–3049, DOI: **10.1021/acs.inorgchem.1c02968**.

39 E. Martínez-Vollbert, C. Philouze, I. Gautier-Luneau, Y. Moreau, P.-H. Lanoë and F. Loiseau, Study of a Phosphorescent Cationic Iridium(III) Complex Displaying a Blue-Shift in Crystals, *Phys. Chem. Chem. Phys.*, 2021, **23**(43), 24789–24800, DOI: **10.1039/d1cp03341g**.

40 D. R. Martir, C. Momblona, A. Pertegás, D. B. Cordes, A. M. Z. Slawin, H. J. Bolink and E. Zysman-Colman, Chiral Iridium(III) Complexes in Light-Emitting Electrochemical Cells: Exploring the Impact of Stereochemistry on the Photophysical Properties and Device Performances, *ACS Appl. Mater. Interfaces*, 2016, **8**(49), 33907–33915, DOI: **10.1021/acsami.6b14050**.

41 P.-H. Lanoë, C. Philouze, N. Vanthuyne, K. Debsouri, J. Crassous and F. Loiseau, Phosphorescent Chiral Cationic Binuclear Iridium(III) Complexes: Boosting the CPL Brightness, *Inorg. Chem.*, 2024, **63**, 24855–24866.

42 A. Barbieri, F. Barigelletti, E. C.-C. Cheng, L. Flamigni, T. Gunnlaugsson, R. A. G. Kirgan, D. Kumaresan, J. P. Leonard, C. B. Nolan, D. P. Rillema, C. Sabatini, R. H. Schmehl, K. Shankar, F. Stomeo, B. P. Sullivan, S. Vaidya, B. Ventura and J. A. G. Williams, *Photochemistry and Photophysics of Coordination Compounds II*, ed. S. Campagna and V. Balzani, Springer, Topics in current Chemistry, 2007, DOI: **10.1007/BFb0047025**.

43 M. Martínez-Alonso, J. Cerdá, C. Momblona, A. Pertegás, J. M. Junquera-Hernández, A. Heras, A. M. Rodríguez, G. Espino, H. Bolink and E. Ortí, Highly Stable and Efficient Light-Emitting Electrochemical Cells Based on Cationic Iridium Complexes Bearing Arylazole Ancillary Ligands, *Inorg. Chem.*, 2017, **56**(17), 10298–10310, DOI: **10.1021/acs.inorgchem.7b01167**.

44 L. K. McKenzie, I. V. Sazanovich, E. Baggaley, M. Bonneau, V. Guerchais, J. A. G. Williams, J. A. Weinstein and H. E. Bryant, Metal Complexes for Two-Photon Photodynamic Therapy: A Cyclometallated Iridium Complex Induces Two-Photon Photosensitization of Cancer Cells under Near-IR Light, *Chem. – Eur. J.*, 2017, **23**(2), 234–238, DOI: **10.1002/chem.201604792**.

45 J. Frey, B. F. E. Curchod, R. Scopelliti, I. Tavernelli, U. Rothlisberger, M. K. Nazeeruddin and E. Baranoff, Structure–Property Relationships Based on Hammett Constants in Cyclometalated Iridium(III) Complexes: Their Application to the Design of a Fluorine-Free FIrPic-like Emitter, *Dalton Trans.*, 2014, **43**(15), 5667–5679, DOI: **10.1039/c3dt52739e**.

46 E. Baranoff, B. F. E. Curchod, F. Monti, F. Steimer, G. Accorsi, I. Tavernelli, U. Rothlisberger, R. Scopelliti, M. Grätzel and M. K. Nazeeruddin, Influence of Halogen Atoms on a Homologous Series of Bis-Cyclometalated Iridium(III) Complexes, *Inorg. Chem.*, 2012, **51**(2), 799–811, DOI: **10.1021/ic2011474**.

47 I. R. Laskar and T.-M. Chen, Tuning of Wavelengths: Synthesis and Photophysical Studies of Iridium Complexes and Their Applications in Organic Light Emitting Devices, *Chem. Mater.*, 2004, **16**(1), 111–117, DOI: **10.1021/cm030410x**.

48 C.-F. Lin, W.-S. Huang, H.-H. Chou and J. T. Lin, Synthesis and Characterization of Cyclometalated Iridium(III) Complexes Containing Pyrimidine-Based Ligands, *J. Organomet. Chem.*, 2009, **694**(17), 2757–2769, DOI: **10.1016/j.jorganchem.2009.04.011**.

49 M. Bregnhøj, F. Thorning and P. R. Ogilby, Singlet Oxygen Photophysics: From Liquid Solvents to Mammalian Cells, *Chem. Rev.*, 2024, **124**(17), 9949–10051, DOI: **10.1021/acs.chemrev.4c00105**.

50 H. Belaidi, S. Belaidi, C. Katan, C. Latouche and A. Boucekkine, Vibronic Coupling to Simulate the Phosphorescence Spectra of Ir(III)-Based OLED Systems: TD-DFT Results Meet Experimental Data, *J. Mol. Model.*, 2016, **22**(11), 265, DOI: **10.1007/s00894-016-3132-8**.

51 R. Schira and C. Latouche, DFT vs. TDDFT vs. TDA to Simulate Phosphorescence Spectra of Pt- And Ir-Based Complexes, *Dalton Trans.*, 2021, **50**(2), 746–753, DOI: **10.1039/d0dt03614e**.

52 C. Xu and W. W. Webb, Measurement of Two-Photon Excitation Cross Sections of Molecular Fluorophores with Data from 690 to 1050 N m, *J. Opt. Soc. Am. B*, 1996, **13**(3), 481–491, DOI: 10.1364/JOSAB.13.000481.

53 S. de Reguardati, J. Pahapill, A. Mikhailov, Y. Stepanenko and A. Rebane, High-Accuracy Reference Standards for Two-Photon Absorption in the 680–1050 Nm Wavelength Range, *Opt. Express*, 2016, **24**(8), 9053, DOI: 10.1364/oe.24.009053.

54 N. S. Makarov, J. Campo, J. M. Hales and J. W. Perry, Rapid, Broadband Two-Photon-Excited Fluorescence Spectroscopy and Its Application to Red-Emitting Secondary Reference Compounds, *Opt. Mater. Express*, 2011, **1**(4), 551, DOI: 10.1364/ome.1.000551.

55 A. Barta, L. Vanwonterghem, M. Lavau, F. Molton, G. Micouin, A.-L. Bulin, A. Banyasz, J.-L. Coll, F. Loiseau, A. Hurbin and P.-H. Lanoë, Monomer *vs.* Dimer of Cationic Ir(III) Complexes for Photodynamic Therapy by Two Photon Activation: A Comparative Study, *ACS Appl. Bio Mater.*, 2025, **8**(5), 4272–4284.

56 F. X. Wang, M. H. Chen, Y. N. Lin, H. Zhang, C. P. Tan, L. N. Ji and Z. W. Mao, Dual Functions of Cyclometalated Iridium(III) Complexes: Anti-Metastasis and Lysosome-Damaged Photodynamic Therapy, *ACS Appl. Mater. Interfaces*, 2017, **9**(49), 42471–42481, DOI: 10.1021/acsami.7b10258.

57 Z. Xu, Z. Yang, Y. Liu, Y. Lu, K. Chen and W. Zhu, Halogen Bond: Its Role beyond Drug–Target Binding Affinity for Drug Discovery and Development, *J. Chem. Inf. Model.*, 2014, **54**(1), 69–78, DOI: 10.1021/ci400539q.

58 P.-H. Lanoë, C. Philouze, N. Vanthuyne, K. Debsouri, J. Crassous and F. Loiseau, Phosphorescent Chiral Cationic Binuclear Iridium(III) Complexes: Boosting the CPL Brightness, *ACS Appl. Bio Mater.*, 2025, **8**(5), 4272–4284, DOI: 10.1021/acsabm.5c00393.

59 M. J. Frisch, G. W. Trucks, H. B. Schlegel, G. E. Scuseria, M. A. Robb, J. R. Cheeseman, G. Scalmani, V. Barone, G. A. Petersson, H. Nakatsuji, X. Li, M. Caricato, A. V. Marenich, J. Bloino, B. G. Janesko, R. Gomperts, B. Mennucci and D. J. Hratch, *Gaussian 16, Revision B.01*, Gaussian Inc., Wallingford CT, 2016.

60 F. Vazart and C. Latouche, Validation of a Computational Protocol to Simulate near IR Phosphorescence Spectra for Ru(II) and Ir(III) Metal Complexes, *Theor. Chem. Acc.*, 2015, **134**(12), 144, DOI: 10.1007/s00214-015-1737-0.

61 C. Latouche, F. Palazzetti, D. Skouteris and V. Barone, High-Accuracy Vibrational Computations for Transition-Metal Complexes Including Anharmonic Corrections: Ferrocene, Ruthenocene, and Osmocene as Test Cases, *J. Chem. Theory Comput.*, 2014, **10**(10), 4565–4573, DOI: 10.1021/ct5006246.

62 C. Latouche, A. Baiardi and V. Barone, Virtual Eyes Designed for Quantitative Spectroscopy of Inorganic Complexes: Vibronic Signatures in the Phosphorescence Spectra of Terpyridine Derivatives, *J. Phys. Chem. B*, 2015, **119**(24), 7253–7257, DOI: 10.1021/jp510589u.

63 C. Latouche, D. Skouteris, F. Palazzetti and V. Barone, TD-DFT Benchmark on Inorganic Pt(II) and Ir(III) Complexes, *J. Chem. Theory Comput.*, 2015, **11**(7), 3281–3289, DOI: 10.1021/acs.jctc.5b00257.

64 J. P. Perdew, K. Burke and Y. Wang, Generalized Gradient Approximation for the Exchange-Correlation Hole of a Many-Electron System, *Phys. Rev. B: Condens. Matter Mater. Phys.*, 1996, **54**(23), 16533–16539, DOI: 10.1103/PhysRevB.54.16533.

65 J. P. Perdew, Density-Functional Approximation for the Correlation Energy of the Inhomogeneous Electron Gas, *Phys. Rev. B: Condens. Matter Mater. Phys.*, 1986, **33**(12), 8822–8824, DOI: 10.1103/PhysRevB.33.8822.

66 A. D. Becke, Density-functional Thermochemistry. III. The Role of Exact Exchange, *J. Chem. Phys.*, 1993, **98**(7), 5648–5652, DOI: 10.1063/1.464913.

67 R. C. Benedetta Mennucci, *Continuum Solvation Models in Chemical Physics: From Theory to Applications*, Wiley, 2008, DOI: 10.1002/9780470515235.

68 B. Mennucci, J. Tomasi, R. Cammi, J. R. Cheeseman, M. J. Frisch, F. J. Devlin, S. Gabriel and P. J. Stephens, Polarizable Continuum Model (PCM) Calculations of Solvent Effects on Optical Rotations of Chiral Molecules, *J. Phys. Chem. A*, 2002, **106**(25), 6102–6113, DOI: 10.1021/jp020124t.

69 J. Bloino, M. Biczysko, F. Santoro and V. Barone, General Approach to Compute Vibrationally Resolved One-Photon Electronic Spectra, *J. Chem. Theory Comput.*, 2010, **6**(4), 1256–1274, DOI: 10.1021/ct9006772.

70 D. Licari, A. Baiardi, M. Biczysko, F. Egidi, C. Latouche and V. Barone, Implementation of a Graphical User Interface for the Virtual Multifrequency Spectrometer: The VMS-Draw Tool, *J. Comput. Chem.*, 2015, **36**(5), 321–334, DOI: 10.1002/jcc.23785.

71 V. Barone, The Virtual Multifrequency Spectrometer: A New Paradigm for Spectroscopy, *Wiley Interdiscip. Rev.: Comput. Mol. Sci.*, 2016, **6**(2), 86–110, DOI: 10.1002/wcms.1238.

72 R. Dennington, T. A. Keith and J. M. Millam, *GaussView Version 6*, 2019.

73 (*a*) CCDC 2091730: Experimental Crystal Structure Determination, 2025, DOI: 10.5517/ccdc.csd.cc286m59; (*b*) CCDC 2091731: Experimental Crystal Structure Determination, 2025, DOI: 10.5517/ccdc.csd.cc286m6b; (*c*) CCDC 2091732: Experimental Crystal Structure Determination, 2025, DOI: 10.5517/ccdc.csd.cc286m7c; (*d*) CCDC 2338300: Experimental Crystal Structure Determination, 2025, DOI: 10.5517/ccdc.csd.cc2jh619; (*e*) CCDC 2338301: Experimental Crystal Structure Determination, 2025, DOI: 10.5517/ccdc.csd.cc2jh62b.